Experimental Study of Rivulet/ Ice Formation by Colour-Coded Point Projection Method

Mohammadali Farzad

A Thesis

in

the Department of

Mechanical, Industrial, and Aerospace Engineering

Presented in Partial Fulfilment of the Requirements

for the Degree of Master of Applied Science (Mechanical Engineering) at

Concordia University

Montreal, Quebec, Canada

August 2019

CONCORDIA UNIVERSITY

School of Graduate Studies

This is to certify that the thesis prepared,

By: Mohammadali Farzad

Entitled: Experimental Study of Rivulet/ Ice Formation by Colour-Coded Point Projection Method

and submitted in partial fulfilment of the requirements for the degree of

Master of Applied Science (Mechanical Engineering)

complies with the regulations of the University and meets the accepted standards with respect to originality and quality.

Signed by the Final Examining Committee:

_____ Chair
Dr. Tsz Ho Kwok

_____ Examiner
Prof. Christian Moreau

_____ Examiner
Prof. Fariborz Haghighat

_____ Supervisor
Prof. Ali Dolatabadi

_____ Co-Supervisor
Dr. Guy Fortin

Approved by:

Dr. Mamoun Medraj
MASc. Program Director,
Department of Mechanical, Industrial and Aerospace Engineering (MIAE)

Dr. Amir Asif
Dean
Gina Cody School of Engineering and Computer Science

Date:

Abstract

Experimental Study of Rivulet/ Ice Formation
by Colour-Coded Point Projection Method

Mohammadali Farzad

Ice accretion on aeroplane surfaces is one of the most severe weather threats to aviation safety. By changing the gross shape of the airfoil and adding surface roughness, ice accretion leads to increased drag and reduced lift at a constant angle of attack. Typically, an Ice Protection System (IPS) protects the critical aerodynamic surfaces. However, ice accreted on unprotected surfaces affects aircraft performance and flight characteristics in some flight phases. Since the formation of different phenomena like rivulets, water runback, and ice ridges is probable, a better understanding of the underlying physics of these complex phenomena is highly desired for both safe and efficient aircraft operation, and better design approaches. Therefore, having an advanced experimental technique capable of quantifying and characterising the amount of water or ice will be of high interest.

In the present study, a novel Colour-Coded Point Projection (CCPP) method is proposed. Using a multi-colour pattern has never been reported in the literature. After calibration and validation, the limitations and characteristics of the proposed method were defined. It can provide three times thickness measurement range at the same planar resolution, in comparison with other similar methods. Various experiments were conducted to investigate the rivulet and ice formation over a NACA 0012 airfoil in the icing wind tunnel available at Concordia University at controlled conditions. The thickness profiles of rivulets and accreted ice were measured successfully and, therefore, the capability of the proposed method was proved. Different criteria, like chord-wise thickness, ice growth rate, advancement speed of ice limit, and the rate of water collection, were defined to compare the effect of working conditions, like velocity, temperature and surface, on the behaviour of rivulets and ice accretion. The results showed that the proposed method is a valuable tool for on-line ice thickness measurements in an icing wind tunnel.

Acknowledgements

First of all, I would like to express my deepest appreciation to my supervisor *Prof. Ali Dolatabadi* for his guidance, great support and kind advice throughout my study. It was a real privilege and an honour for me not only to share his exceptional scientific knowledge but also of his extraordinary human qualities.

I also would like to thank my co-supervisor *Dr. Guy Fortin* for his constant help, availability and constructive suggestions, which were determinant for the accomplishment of the work presented in this thesis.

I have been extremely lucky to have such supervisors who cared so much about my work, and who responded to my questions and queries so promptly. Their advice has been priceless to me.

To my colleagues and friends of the *Thermal Spray and Multiphase Flow Laboratories* in the *Department of Mechanical, Industrial and Aerospace Engineering*, I thank them for their companionship and for providing a so pleasurable and friendly working atmosphere.

Specially, I am really thankful to my friend *Dr. Mehdi Jadidi*, who was always ready to help me when I needed any guidance.

Last, but not least, I would like to thank my family for their unconditional support and encouragement, without which I would not have come this far.

To my wife, Fariba, for her keen interest, encouragement and spiritual support during my study and her unconditional love in all the moments of life. All the burdens of life were on her during my graduate studies.

To my late parents for their great role in my life and their numerous sacrifices for me. This thesis is dedicated to their souls.

TABLE OF CONTENTS

LIST OF FIGURES

LIST OF TABLES

NOMENCLATURE

Parameter	Description	Unit
$\overline{AB}$	: Point displacement	pixels
C	: Chord size	mm
d	: Projector-camera horizontal spacing	mm
h	: Thickness	mm
I	: Image intensity map	---
K	: Calibration coefficient	mm/pixels
L	: Vertical distance between substrate and camera and projector	mm
LWC	: Liquid water content	g/m^3
MVD	: Mean volume diameter	μm
R	: Correlation coefficient	---
S	: Span size	mm
T	: Temperature	^oC
t	: Time	s
X	: Chord-wise location	mm
Y	: Span-wise location	mm

Abbreviations

CC	: Cross-Correlation
CCPP	: Colour-Coded Point Projection
DIC	: Digital Image Correlation
DIP	: Digital Image Projection
FFP	: Fast Fourier Profilometry
FTP	: Fourier Transform Profilometry
IPS	: Ice Protection System
LWC	: Liquid Water Content
MVD	: Mean Volume Diameter
NTSB	: National Transport Safety Board
PIV	: Particle Image Velocimetry
PSD	: Position-Sensitive Device
PSP	: Phase Stepping Profilometry
ROI	Region Of Interest
SNR	: Signal to Noise Ratio

1 Introduction

1.1 Background and Motivation

Nowadays, aeroplanes are the safest machines ever created and have been designed to keep working even if things go wrong. They contribute hugely to the transportation of passengers and goods. Just over four billion passengers were transported in 2018, which had almost doubled since 2008. Although wide safety margins are usually applied in design and operation, failure is also probable. This probability may originate from either human error or working conditions.

One of the most critical working parameters in aviation safety is the weather. The contribution of weather-related accidents among over 20,000 aviation incidents in the period of 2000-2011 was about 29% [1]. Figure 1-1 shows the contribution of different problems for aviation safety due to the weather. Among these issues, icing has attracted the attention of engineers and researchers since the invention of aeroplanes. Besides the contribution of icing-related issues in aviation accidents, its effect on the operational efficiency of aeroplanes is also significant. Therefore, research in this area is still intensive.

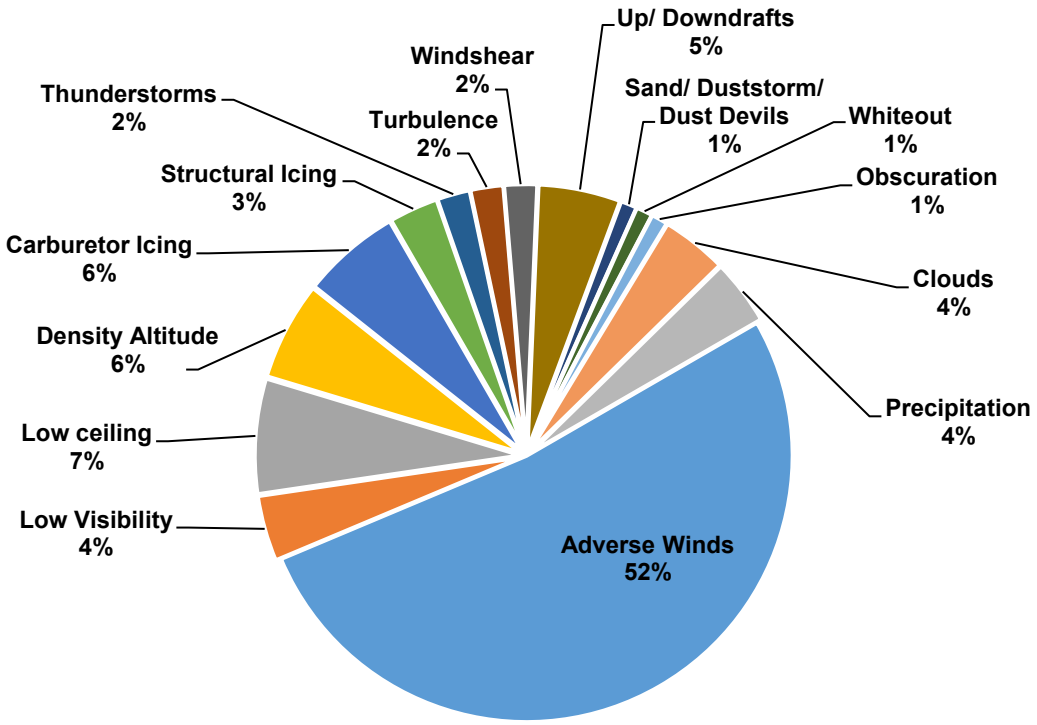

Figure 1-1: Contribution of different causes of weather-related accidents in the aviation industry (reproduced from [1]).

Aircraft icing can be categorised as structural or induction. The former refers to ice forming on aircraft surfaces and components, when supercooled droplets adhere to them and freeze. This is the primary concern for this research. The latter is about ice formation in the engine's induction system. Figure 1-2 shows the effects of icing on an aeroplane schematically. While the effect of additional weight is negligible, the effect on aerodynamic performance may be severe. By changing the gross shape of the airfoil and adding surface roughness, ice accretion leads to increased drag and reduced lift at a constant angle of attack. It may change the pressure over the airfoil and, consequently, affect its aerodynamic behaviour, even before the stall. Some stability and control problems were also reported on an ice-contaminated horizontal tail [2]. Furthermore, it has adverse effects on roll control (e.g., ailerons), pitching moments (e.g., tailplane), thrust (e.g., propeller), and instrumentation (e.g., pitot tube and static ports).

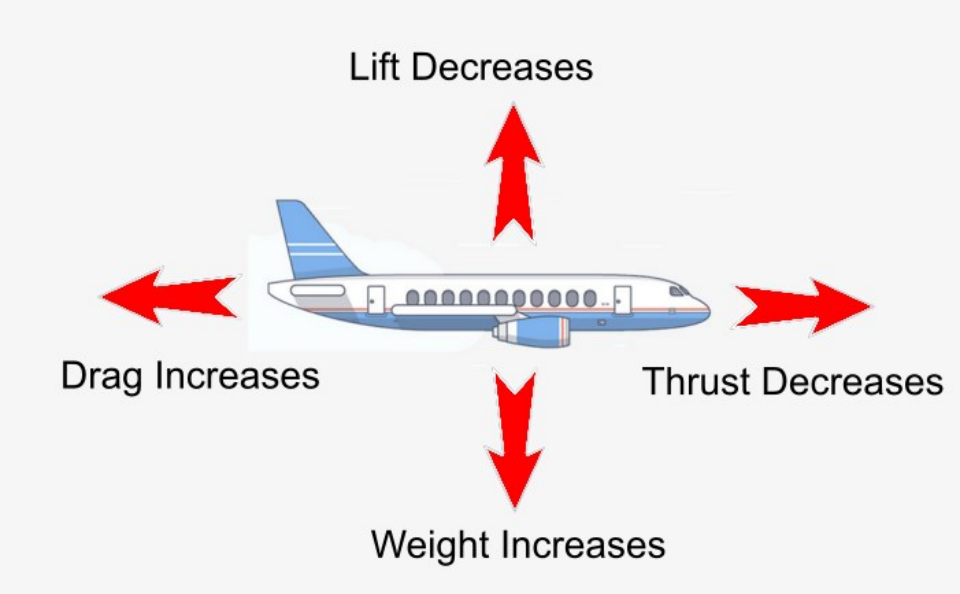

Figure 1-2: Effects of icing on the aerodynamic performance of aeroplanes.

Figure 1-3 compares the effect of icing on the lift and drag coefficients on a typical airfoil (e.g., wing or tailplane). Ice contamination reduces the maximum lift coefficient significantly and lowers the stall angle of attack. In terms of safety, reduced maximum lift coefficient and increased stalling speed may produce dangerous situations in take-off and landing. During the approach, while the pilot is slowing down and increasing the angle of attack, he may find that the ice on the wing, which had little effect on the lift during the cruise, now is leading to a stall condition. Even a thin layer of ice at the leading edge increases the stall speed. The situation may be worse when accretion is on unprotected areas. A reduction of maximum lift coefficient by 30% is usual, and it may reach 40-50% in a large-horn ice accretion [3]. Even small ice accretion causes a significant reduction in maximum drag coefficient and again lowers the stall angle of attack. In this situation, the effect on the drag coefficient is more significant at small angles of attack. The drag steadily increases as ice accretes. Therefore, 100% drag increase is usual and can be 200% or even higher in a large-horn ice accretion [3].

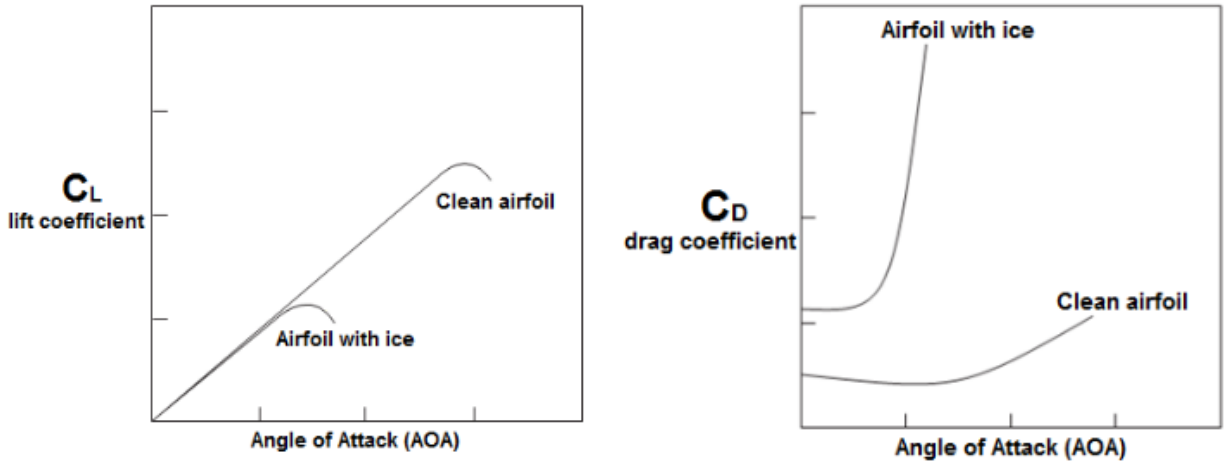

Figure 1-3: Typical effects of ice contamination on lift and drag coefficients in different angles of attack [3].

Different approaches have been implemented to eliminate or postpone the formation on an aeroplane's components. They range from merely spraying anti-icing fluid before the flight to more sophisticated systems, like pneumatic boots, thermal ice protection systems (using either engine bleed air or electro-thermal elements), and electro-impulse systems. Although these systems work well, they have some drawbacks, such as high initial cost, additional weight, and maintenance complexity [4]. The engine bleed air thermal protection system, which is used widely in commercial aviation, is limited in size and power. New environmental regulations or fuel consumption concerns limit the bleed air temperature to a lower level than previously. Therefore, the tendency is to use these systems as little as possible, and many airfoil surfaces may remain unprotected. As a result, less water evaporates and more runs back. As shown in Figure 1-4, the water runs back in a wet regime as a thin film, and then breaks into rivulets and sometimes to beads. These rivulets or beads move backwards on the cold surface and freeze downstream, e.g., between the slat's leading edge and the wing's trailing edge. The subsequent ice formation changes the airfoil shape drastically and produces large regions of flow separation aft of the ice horns, which, consequently, increases the drag severely, reduces the maximum lift coefficient and changes the pitching moment to some extent [4].

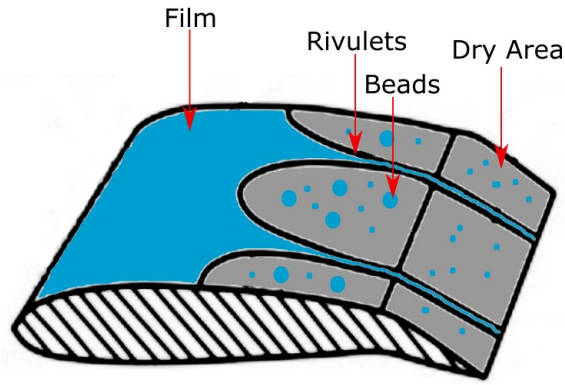

Figure 1-4: Schematic of thin-film, rivulets, and bead on an airfoil.

1.2 Ice Accretion Mechanism

Three meteorological parameters mainly determine the type and severity of ice accretion, which are the Liquid Water Content (LWC), the temperature, and the droplet size. The liquid water content depends on the size and amount of droplets in a given volume. The higher the LWC, the higher the icing potential. It is also a key parameter in the rate of ice accretion. Generally, LWC is in the range of 0.1-3 g/m^3 [5]. The role of temperature is vital in in-flight icing, as well. The most significant threat in icing conditions occurs in the range of -15°C to 0°C, since most of the droplets are still in the liquid (supercooled) state [6]. Droplet size is another critical parameter in icing, which is in the range of 10-50 µm in clouds [5]. On some occasions, droplets much larger than 50 µm (even up to 400-500 µm) remain in the cloud. These are called large supercooled droplets and are a considerable icing hazard [5]. Typically, the droplet size and temperature determine the type of icing, while LWC (and droplet size, to some extent) accounts for the rate of accretion and the severity of the icing encounter [6].

Depending on the atmospheric and flight conditions, the type of the ice is different in terms of structure and appearance, as shown in Figure 1-5. Relatively slow freezing forms glaze ice. It is glossy, transparent, denser, and harder to remove. Due to difficulties in observation and removal, glaze ice is the most dangerous type of ice accretion [6]. On the other hand, rime ice is rough and milky, which forms by the too rapid freezing of the supercooled droplets. Since air cannot escape, air pockets present in the ice and make it opaque, rough, porous, and brittle. In some situations, a mixture of the ices mentioned above is also possible to form, which is called mixed ice. Because

it is a mixture of glaze and rime ice, it may be transparent or opaque. It is more adhesive than rime ice, in general. Table 1-1 illustrates the characteristics of different types of ice.

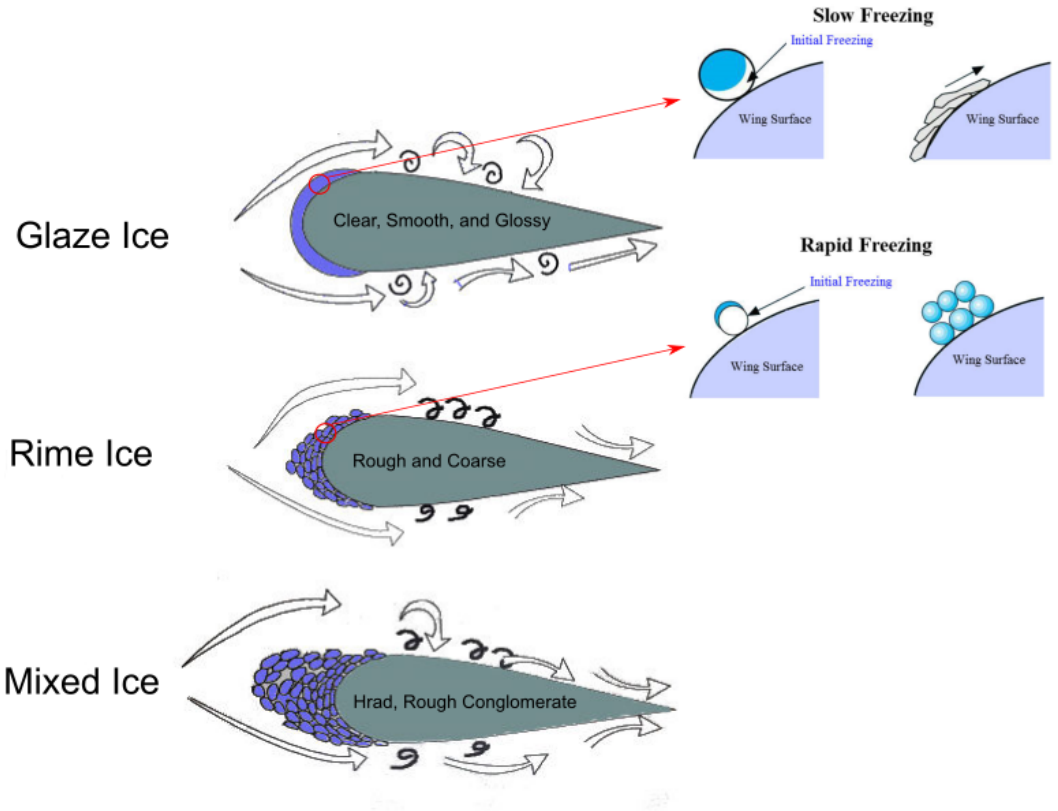

Figure 1-5: Different types of ice in the icing condition (reproduced from [7]).

Table 1-1: Summary of favourite conditions and level of risk for different types of ice [3].

Parameter	Glaze Ice	Rime Ice	Mixed Ice
Temperature (°C)	-10 to 0	-40 to -15	-15 to -10
Droplet Size	Large	Small	Both
Liquid Water Content	High	Low	In between
Risk	High	Low	Intermediate

One way to mitigate icing problem, by counteracting the formation of ice (anti-icing) or ensuring easier removal of the accreted ice (de-icing), is coating the surface with superhydrophobic materials. The interaction between water and a solid surface is characterised by the static contact angle and the contact angle hysteresis, as shown in Figure 1-6. A superhydrophobic surface has a

contact angle more than 150° (provides water repellency) and a contact angle hysteresis less than 10° (provides water mobility). Although a superhydrophobic surface is not generally icephobic due to the coating's roughness, it is beneficial in mitigating the re-freezing of runback water on unprotected areas of the aeroplanes. This capability is shown in Figure 1-7, in which the heater at the leading edge melted the formed ice, but water froze again on bare unprotected areas. Using a superhydrophobic coating eliminates re-freezing and keeps the surface dry.

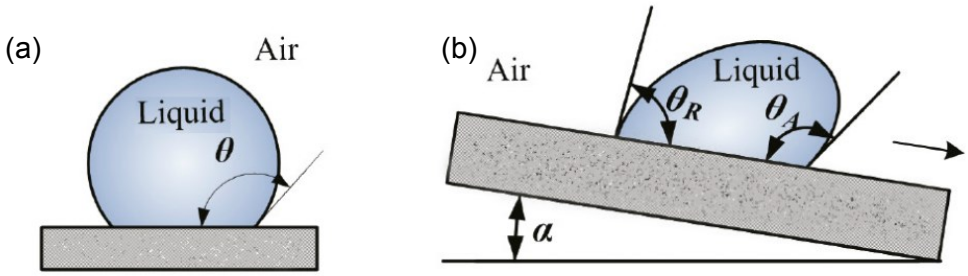

Figure 1-6: (a) Static contact angle (θ), and (b) Contact angle hysteresis (θ_A-θ_R).

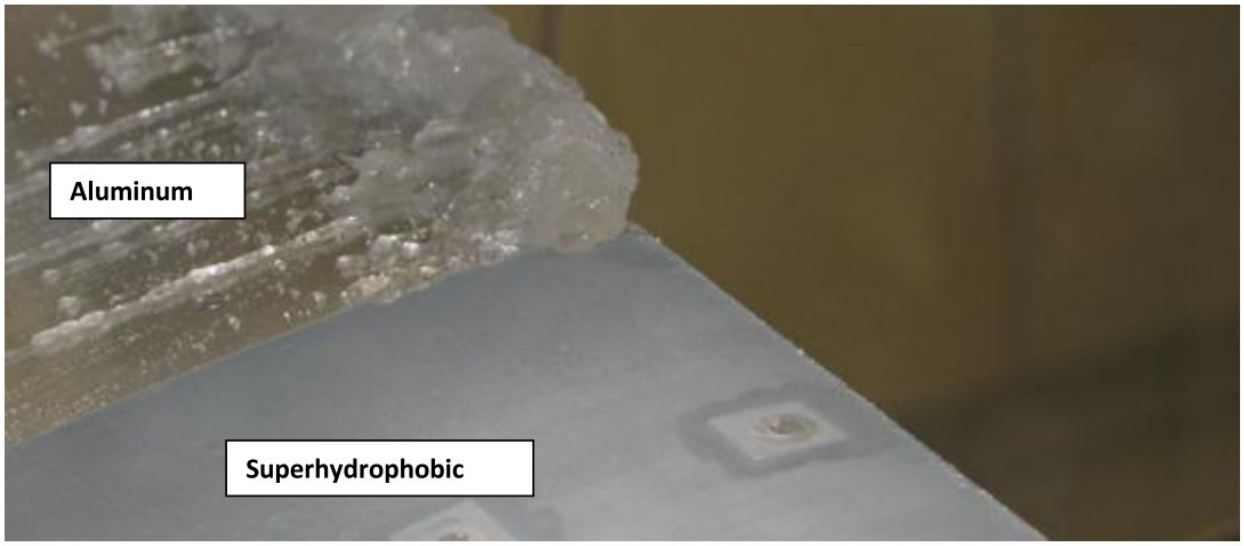

Figure 1-7: Difference in ice accretion between an aluminium and superhydrophobic surface on an airfoil having a heating element at its leading edge [8].

1.3 Free-Surface Measurement Methods

3D characterisation of runback rivulet flow/ ice formation is a particular case of free-surface measurement. These methods themselves are customised versions of more general

techniques in metrology and 3D scanning. Different phenomena in various fields, such as lava flow in geology, lubricant oil film in tribology, surface coating, manufacturing and protection of microchips, and icing on aircraft and wind turbines, can be characterised by these techniques [9].

Early experiments in film flow characterization mainly relied on visual comparison of flow from snapshots and measuring the contact line displacement by means of either a graded surface [10][11][12][13][14] or image processing tools [15][16][17][18]. Figure 1-8 shows some typical examples of the experiments before advent of the advanced profile mapping methods. Lack of more detailed information, such as film thickness and contact line's moving velocity, is the reason for interest in new free-surface measurement methods. Several methods have been proposed to study the behaviour of the free-surface flow. Some of them will be discussed below.

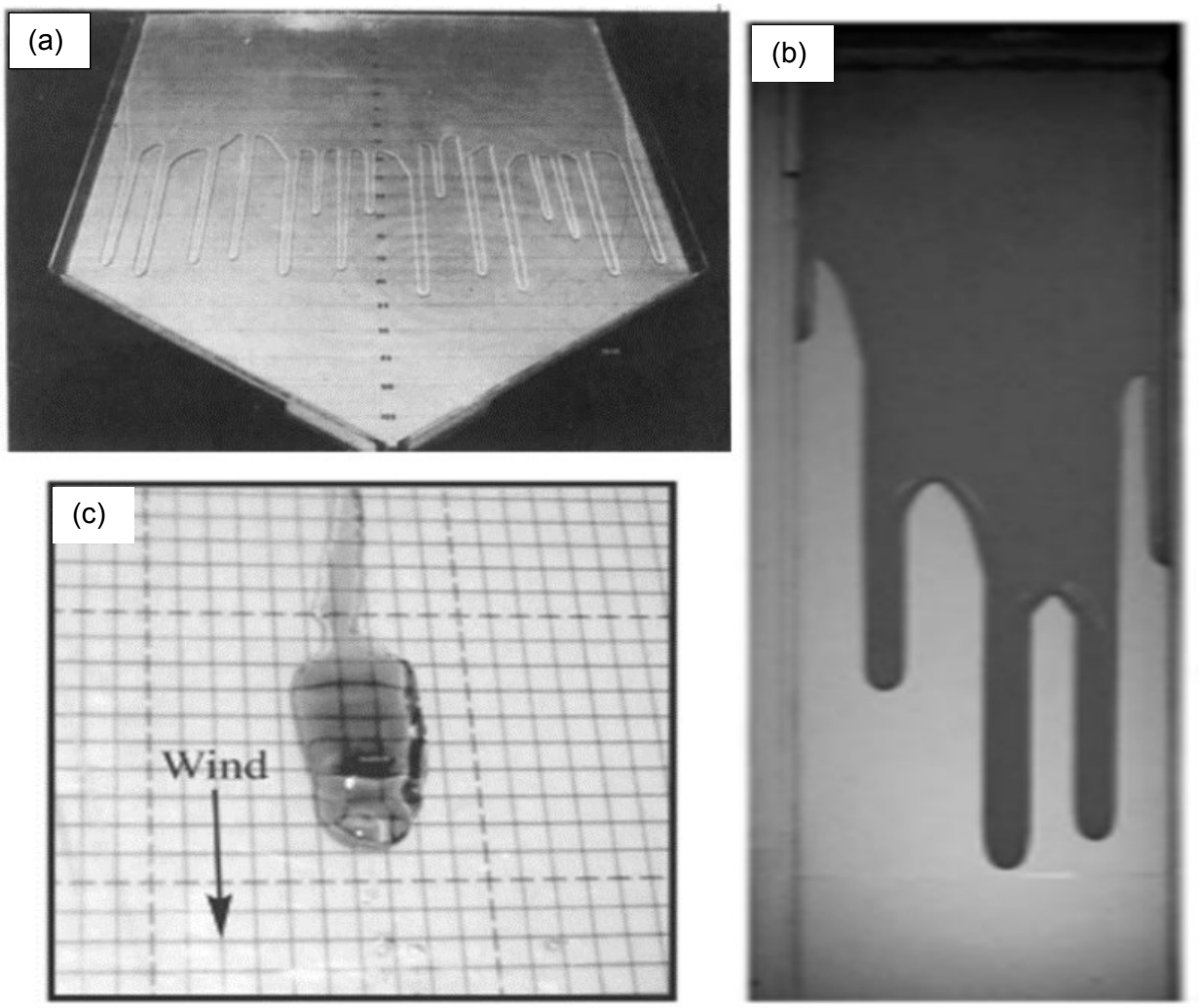

Figure 1-8: Different flow characterisation methods. (a) Film flow on a sloped sheet using graded surface [11], (b) Film flow on a sloped sheet using image processing [15], and (c) wind-driven rivulet flow using graded surface [13].

The chromatic confocal imaging technique is typically applies to measure the surface structure of solid objects. As shown in Figure 1-9, a point source of polychromatic light passes through a lens and is split into a continuum of monochromatic beams with focal points at different distances. Then the reflections from the surface are conducted to a spectrometer in which the intensity of the light spectrum is converted to a signal. By analysing the peak location in each wavelength, a corresponding map of the object's surface profile can be extracted. The main limitation of this method is that it is a single-point measurement. Furthermore, it needs an opaque surface with uniform optical properties. In addition, the experimental setup is complicated and

expensive. Lel et al. [19] used this method to measure the thickness and wave velocity of a wavy film.

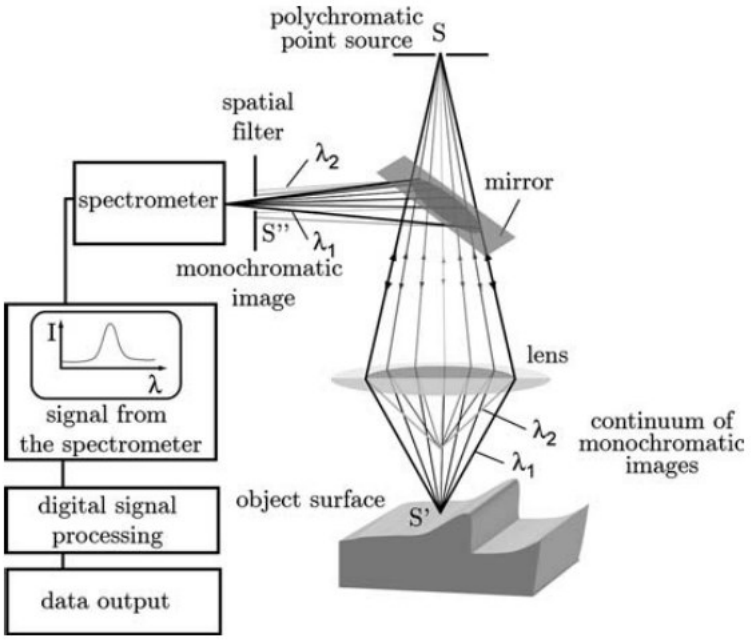

Figure 1-9: Schematic of chromatic confocal imaging [19].

The stereoscopic imaging technique is frequently used in distance measurement and 3D reconstruction. The concept of this method is shown in Figure 1-10. Two cameras observe the object under study from different perspectives. The pair of captured images are matched using Digital Image Correlation (DIC). The information about the third dimension is then extracted utilising the triangulation concept. The essential factor in this method is that the object must have some distinct features (e.g., edges, crosses, circles) to be used for matching. Since it is difficult for a liquid surface to provide such features, a seeding material must be added. It may be either real seed materials or a random pattern projected on the surface. The complicated and time-consuming matching algorithm is the main drawback of this method. This method was exploited by Benetazzo [20] to measure sea wave elevations and by Eaket et al. [21] to study dam-break flow. Tsubaki and Fujita [22] improved this method by adding a projector to project an irregular pattern of light to reach a higher level of accuracy. Wanek and Wu [23] added a third camera to the system to assist the matching process.

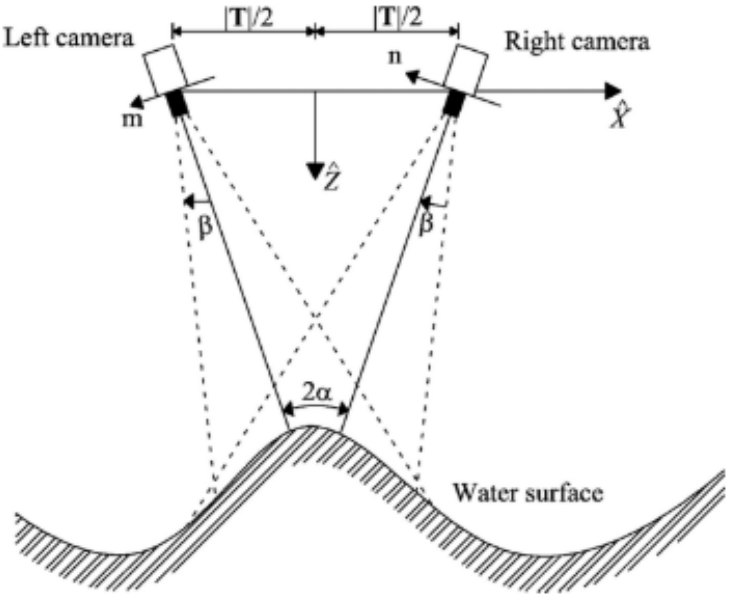

Figure 1-10: Typical schematics of stereoscopic imaging [20].

Structured light projection is a broad category of shape measurement techniques. It has been applied successfully in many fields, such as 3D sensing, object recognition, robot control, industrial inspection, reverse engineering, stress/strain measurements, and biometrics [9]. As shown in Figure 1-11, it is based on the projection of a pattern with specific characteristics on the object under study and then observing the object with a digital camera from another view. The geometry of the object deforms the projected pattern. Analysing the deformed pattern then provides information regarding the object's geometry. Although different patterns were proposed for this technique, the fringe pattern is common [24]. Fourier Transform Profilometry (FTP) and Phase Stepping Profilometry (PSP) are most common decoding methods for fringe patterns [25]. Although PSP is not practical for dynamic phenomena, FTP works well. However, it needs the camera to be accurately synchronised with the projector. The decoding algorithm is straightforward for both, but the profile reconstruction is too tricky in real cases, especially in the presence of a discontinuity. These discontinuities originate from shadows or sharp edges and propagate throughout the solution domain. Eliminating them is still an open research area in computer science. Time-consuming gamma correction is another limitation of this method. Zhang and Su [26] used FTP to reconstruct the vortex shape at a free surface. This method was employed to characterize the deformation of granular flow [27], measure the time evolution of flow on an

inclined surface due to a dam break [28], measure water waves [29], characterize the transient behaviour of droplet/ rivulet flow [9], and study the storm overflow of a sanitation system [30].

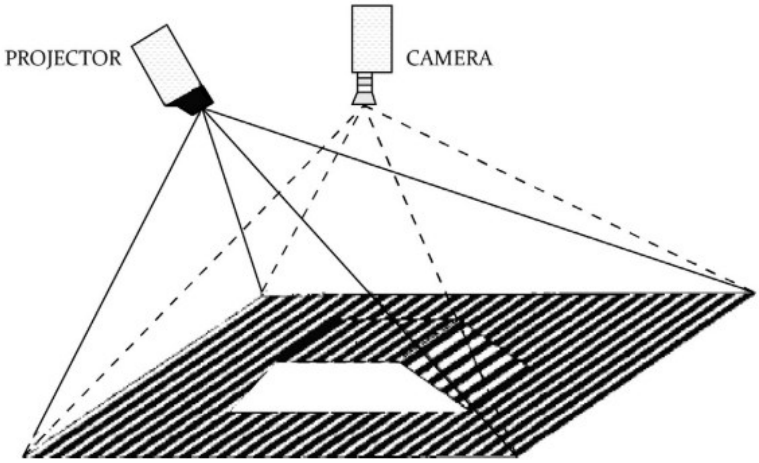

Figure 1-11: Typical schematics of structured light projection [24].

The fluorescent imaging technique is based on doping the fluid with a small concentration of fluorescent dye and observing the flow under ultra-violet light, as shown in Figure 1-12. The fluorescent intensity is proportional to the film thickness. A UV lamp, laser, or LED generates the fluorescent excitation, while the observation is accomplished with a CCD camera. Light scattering in the liquid film produces saturated regions in the captured image. Therefore, this method is not suitable for studying small objects, like shear-driven rivulets on airfoils. Liu et al. [31] measured the dynamic film thickness variations in gravity-driven film flows. Then, Johnson et al. [32][33] studied rivulet formation on a sloped plate. Chinnov et al. [34], Schagen and Modigell [35] and Hidrovo and Hart [36] are other examples.

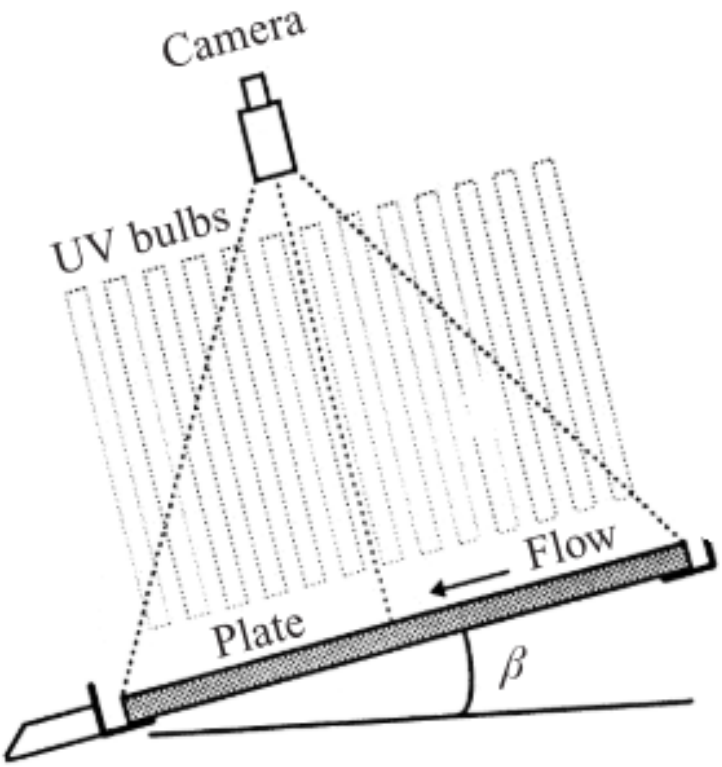

Figure 1-12: Typical schematics of fluorescent imaging technique [33].

In a density-based method, as shown in Figure 1-13, an array of light sources is located under the water container, illuminating the surface. A camera looks downward and observe the surface. The light beams coming from the source are refracted at the surface. The existing intensity is inversely proportional to the local depth. If the undisturbed surface is in focus, then the darker regions are higher, and the lighter ones are lower than the reference surface. The requirement for back-illumination makes it impractical for studies on airfoils. Furthermore, ice formation blocks the light. Thus, this method can be implemented just for liquids. Wright et al. [37] used this method to study turbulence on the water surface. Zhang et al. [38] developed a density-based colour light encoding technique to measure free-surface deformation due to turbulence. Kabov et al. [39] and Moisy et al. [40] used this method to study rivulet structures in a falling liquid thin film and liquid interface topography, respectively.

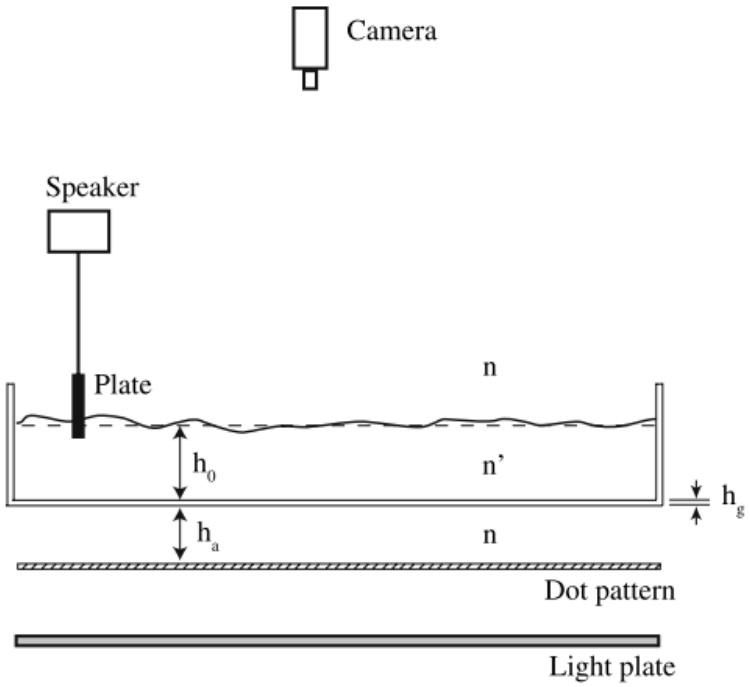

Figure 1-13: Typical schematics of a density-based method [40].

Refraction is the basis of a laser scanning technique. In this method, a laser beam is sent perpendicularly through the bottom of the substrate, as shown in Figure 1-14. The beam refracted when it reaches the surface. A set of lenses then collect the refracted beam and guide it to a so-called Position-Sensitive Device (PSD) which produces four signals. The ratios of these signals determine the location of the laser spot. By sweeping the object under study and locating each laser spot, a map is constructed. The beam displacement is a measure of the slope (gradient) of the surface. This information can be used to reconstruct the object shape. Complexity and expensive experimental setup are the main drawbacks of this method. Furthermore it cannot provide multiple measurements at the same time. Therefore, the study of dynamic objects is impossible. Savelsberg et al. [41] used this method to characterise a turbulent free surface. The same concept was used by Pautsch and Shedd [42] to measure the liquid film thickness on an electronic chip during spray cooling.

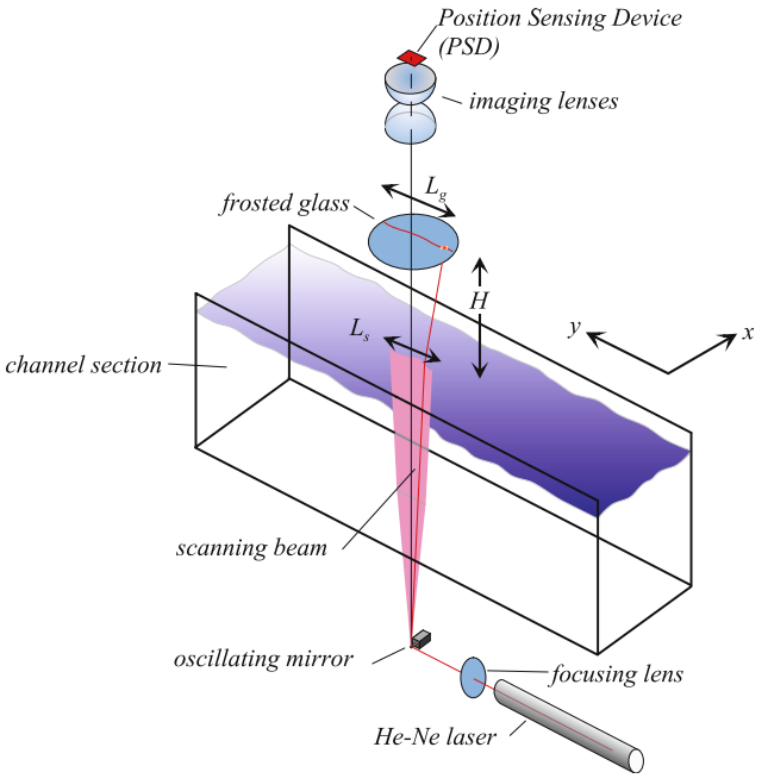

Figure 1-14: Typical schematics of laser scanning [41].

Another method, which recently has been proposed for studying rivulet flow, is Digital Image Projection (DIP). It is a particular version of a structured light projection technique, and its experimental setup is shown in Figure 1-11. Instead of projecting a continuous pattern, one with discrete features is used in this method. By analysing the features locally, the problem of error propagation is completely solved. If the desired time resolution is not very fine, the necessity of synchronisation can also be eliminated to some extent. One of the main limitations of this method is its limited thickness measurement range. There is always a trade-off between the thickness measurement range and the planar resolution. If the planar resolution is set for a specific object's thickness, variations on thickness cannot be more than 50% of the set value. Therefore, it is not practical for measuring growing objects, such as ice. Zhang et al. proposed this method and used it to study wind-driven water film flows on a flat surface [43], and thin-film and rivulet flow on an airfoil [44][45]. This method will be discussed in detail in chapter 2.

Despite the importance of studying the behaviour of fluid film, droplets, rivulets, and ice in wind tunnel experiments, a gap is found in the literature among free-surface measurement

methods. A summary of the surveyed methods is shown in Table 1-2. The usual practice for ice thickness measurement in wind tunnel experiments is either to use manual measurement tools (micrometre) or to scan the formed ice (hand scanners). This implies that the experiment needs to be stopped, and in some cases, the sample to be removed from the test section. An ideal measurement method must be whole-domain and can capture the dynamic behaviours of the phenomena. It must not be constrained by the object's size and optical properties. The equipment also has to be kept as simple as possible. Therefore, a compatible and simple thickness measurement method is highly demanded.

Table 1-2: Summary of different free-surface measurement methods.

	Domain	Motion Capture	Object's Size	Surface	Cost	Analysis
Chromatic confocal imaging	Single-point	Impossible	Small to medium	Opaque	Expensive	Complicated
Stereoscopic imaging	Whole-domain	Possible	Small to big	Opaque (with distinct features)	Low Cost	Moderate
Structured light projection (FTP)	Whole-domain	Possible (required synchronisation)	Small to big	Opaque	Low Cost	Moderate to complicated
Structured light projection (PSP)	Whole-domain	Impossible	Small to big	Opaque	Low Cost	Easy to moderate
Fluorescent imaging	Whole-domain	Possible	Medium to big	Transparent	Moderate	Easy to moderate
Density-based methods	Whole-domain	Possible	Medium to big	Transparent	Low Cost	Easy to moderate
Laser scanning technique	Single-point	Impossible	Small to big	Transparent	Expensive	Complicated
Digital Image Projection	Whole domain	Possible	Small to medium	Opaque	Low Cost	Easy to moderate

1.4 Objectives

The objective of this study is to improve and develop an on-line, dynamic, and non-intrusive method to measure the thickness of water rivulets and formed ice on an airfoil surface. The study further expands to compare the effect of different working conditions (like velocity, temperature, and surface) on the behaviour of rivulet/ ice formation. This objective is outlined below:

- Extending the concept of the DIP technique to improve the thickness measurement range by introducing the CCPP technique.
- Characterizing the CCPP technique for water/ ice thickness measurement in wind tunnel experiments.

In chapter 2, the fundamentals of CCPP technique and the experimental setup are presented in detail. Then, the thirds chapter is devoted to the experimental results, including the technique characterisation and wind tunnel tests. Finally, in chapter four, some practical notes, limitations of this method, and the open areas for future researches are discussed.

2 Methodology

This chapter is devoted to the methodology implemented in this study and divided into two sections. The first part describes the fundamentals of the Colour-Coded Points Projection (CCPP) method, which is an improved version of Digital Image Projection (DIP). This part includes the optical principles and algorithm of both DIP and CCPP. Then the calibration and validation practices are discussed. The second section covers the experimental setup. The parameters of the wind tunnel tests are then specified. Furthermore, the required settings for the CCPP are discussed.

2.1 CCPP Fundamentals

The Colour-Coded Points Projection (CCPP) method is based on structured light triangulation. It needs a projector, a camera, and analyser software. The projector projects a pattern with specific characterisations on the object under study. The projected pattern looks distorted in the camera view due to the geometry of the object. Two images then are taken, one from intact pattern (reference image) and another from the distorted one (object image). The software analyses the captured images and reconstructs the object's geometry. Comparing the intact pattern with the distorted one using the cross-correlation technique is the heart of the software.

2.1.1 Optical Principle

Figure 2-1 illustrates the typical configuration of the CCPP setup. The projector and the camera are standing at the distance L from the substrate, while the horizontal spacing between

them is d. P and C represent the locations of the projector's light source and the camera's sensor, respectively. The projector ray strikes the object's surface at point S and reflects back toward the camera. Assuming there is no object on the surface, point S has two corresponding locations on it; point B from the projector perspective and point A in the camera view. Since SPC and SAB triangles are similar, the following relationship is deduced:

$$\frac{h(x,y)}{\overline{AB}} = \frac{L - h(x,y)}{d} \tag{2-1}$$

where $h(x,y)$ is the height of the object at (x,y). $\overline{AB}$ is the point displacement which can be estimated by analysing the reference and the object images.

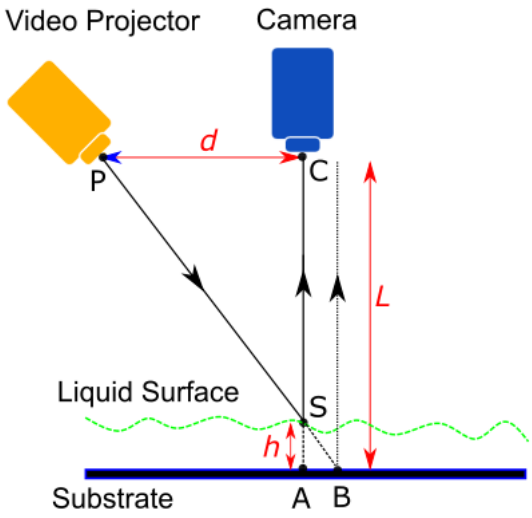

Figure 2-1: Schematic of the CCPP setup.

By rearranging equation (2-1), we have:

$$h(x,y) = \frac{L.\overline{AB}}{\overline{AB} + d} \tag{2-2}$$

Since $\overline{AB} \ll d$, then $\overline{AB} + d \cong d$. Therefore, we have:

$$h(x,y) = \frac{L}{d}\,\overline{AB} \tag{2-3}$$

Because L and d are constants of the experimental setup, it is deduced that the relation between the height of the object and point displacement is linear. However, the lack of information about the exact locations of the camera's sensor and the projector's light source makes finding the exact configuration difficult. In addition, the relative location of each point on the object to the camera/projector is slightly different from the others. Therefore, instead of using just a simple conversion coefficient, a conversion map, $K(x,y)$, is required for the domain of study.

$$h(x,y) = K(x,y)\,\overline{AB} \tag{2-4}$$

The procedure of finding $K(x,y)$ is the subject of the calibration step. What is unknown so far is the point displacement, which is measured using the cross-correlation algorithm.

As depicted in Figure 2-2, the main difference between the proposed method and DIP is the structure and colour of the pattern. In the DIP method, the pattern is a black and white grid, while a set of colourful points are projected in the CCPP method. The points in CCPP can be in any arrangement, unlike DIP, which needs a regular and structured pattern. The main benefit behind this modification is reducing the fictitious data. These errors originate from the grid overlapping. Therefore, the need for a sophisticated validation procedure can be eliminated. The thickness measurement range of both methods is limited by the distance between two adjacent grids. Therefore, there is a trade-off between the planar resolution and the thickness measurement range. This novel method encodes the adjacent features (points) by colour. The implemented version of this method only uses three colours. However, more colours and different patterns can be employed. By using the three-colour scheme, the thickness measurement range is increased by three times with the same equipment and at the same planar resolution, in comparison to the DIP method.

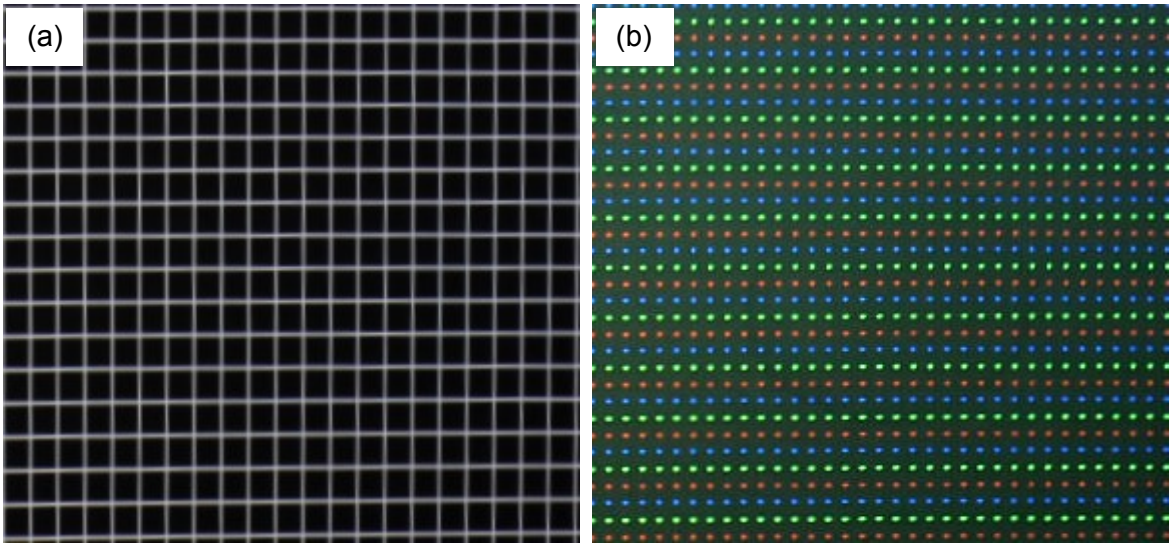

Figure 2-2: Comparison of the projected patterns; (a) DIP versus (b) CCPP.

The procedure of analysing the captured images is divided into four steps: i) finding the location of points in the reference image, ii) finding the new location of each point in the object image, iii) calculating the displacement of each point, and iv) converting the displacement to thickness. The CCPP method, like its ancestor, uses the concept of cross-correlation to find the displacement between the reference and the object images. Since each point is analysed locally, errors do not propagate throughout the whole domain and then can be detected and eliminated. Errors may originate from low quality images or local defects such as shadows and light speckles.

2.1.2 Cross-Correlation Concept

The Cross-Correlation (CC) concept is the heart of various analysing algorithms. In simple words, this concept measures the similarity between two sets of data. In the field of mechanical engineering, CC is widely used in Digital Image Correlation (DIC) and Particle Image Velocimetry (PIV). While the former is used to reconstruct the strain map for a solid object under stress, the application of the latter is in the velocity profile measurement of moving gases.

The fast normalised cross-correlation algorithm from Lewis [46] is implemented in the search algorithm of CCPP. Figure 2-3 shows a schematic of this concept. At first, a neighbourhood of a feature in the reference image is selected, which is called the source window (I_r). This window has a counterpart on the object image, which is called the roam window (I). The roam window is

inside a bigger area (search window) in which the similarity is likely to be found between it and the source window. The amount of similarity between the source window and roam window is calculated by the following equation:

$$R(\Delta x, \Delta y) = \frac{\sum_{x,y}[I_r(x,y) - \bar{I}_r][I(x-\Delta x, y-\Delta y) - \bar{I}]}{\sqrt{\sum_{x,y}[I_r(x,y) - \bar{I}_r]^2 + \sum_{x,y}[I(x-\Delta x, y-\Delta y) - \bar{I}]^2}} \quad (2\text{-}5)$$

where I_r and I are the image intensity within the source window and roam window, respectively. The overbar operator means the mean intensity in the corresponding window. $R(\Delta x, \Delta y)$ is the correlation coefficient, which is in the range of [-1, 1]. A value near zero means the least similarity, while approaching unity represents maximum resemblance. Δx and Δy determine the relative displacement vector of the roam window from the source window.

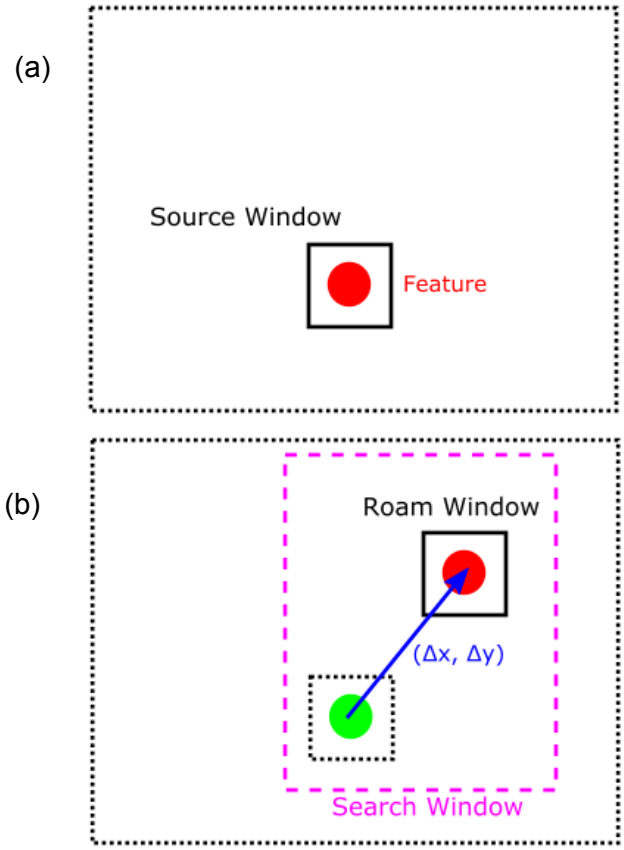

Figure 2-3: Schematic of the cross-correlation technique. (a) The first image with highlighted source window and (b) The second image with the search window and the probable location of the source window (Roam window).

By examining all areas in the search window, a correlation map is reconstructed, as shown in Figure 2-4. The location of the peak in the correlation map corresponds to the most probable location of the feature in the second image. Thus, by using this technique for every well-defined search window around the features in the whole image, the displacements of all chosen features are estimated. The maximum displacement must be kept less than half of the grid spacing, to make sure not to detect fictitious correlations with neighbouring features [47]. Therefore, there is always a trade-off between planar resolution and the measurement range.

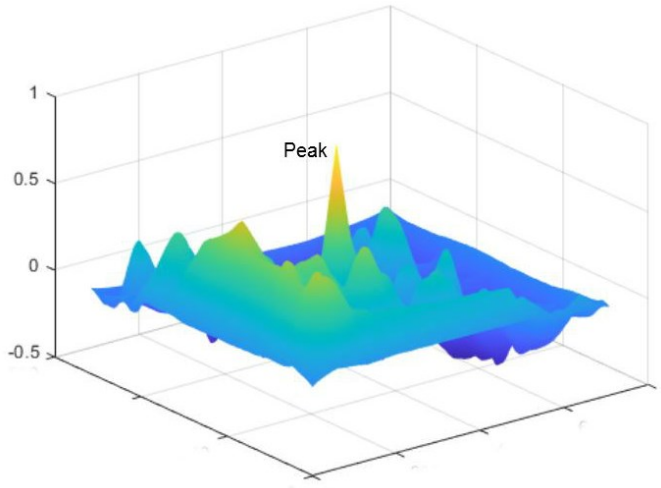

Figure 2-4: Typical representation of correlation map [48].

The accuracy of the method is just one pixel so far. Fitting a surface to the correlation coefficient map provides sub-pixel accuracy. As expressed in equation (2-6), a fourth-order polynomial surface $F(x, y)$ was chosen to fit on the 5×5 neighbourhood of the peak in each search window:

$$F(x,y) = \sum_{n=0}^{4} \left(c_{n,0}\, x^n\, y^0 + c_{n,1}\, x^n\, y^1 + \cdots + c_{n,n}\, x^n\, y^n \right) \tag{2-6}$$

where x and y are relative coordinates regarding the location of the peak and $c_{i,j}$ are fit coefficients. A non-linear least-square algorithm calculates these coefficients. The fit domain was discretised into 100 intervals.

A typical result for reconstruction of a water droplet is shown in Figure 2-5. Part (a) shows the reference image and the point pattern as the search features. The original location of each point is found using a pattern detection algorithm. Part (b) represents the object image, in which the displacement of the dots is apparent. Finally, part (c) shows the displacement vector map. In this figure, the location of the projector is at the bottom side of the probing area and the camera is perpendicular to the surface. A closer look at Part (b) reveals the presence of a light speckle on the surface of the droplet, which can be a source of error. In the case of a large damaged area, it affects the measurements in its vicinity. The probability of error at the edges of the object is usually high, especially when a part of the point is on the liquid surface and the rest is on the substrate surface. This problem gets worse at the edges far away from the projector, like the upper edges in part b. If either the thickness or its gradient is high in these regions, shadows or overlapping may occur.

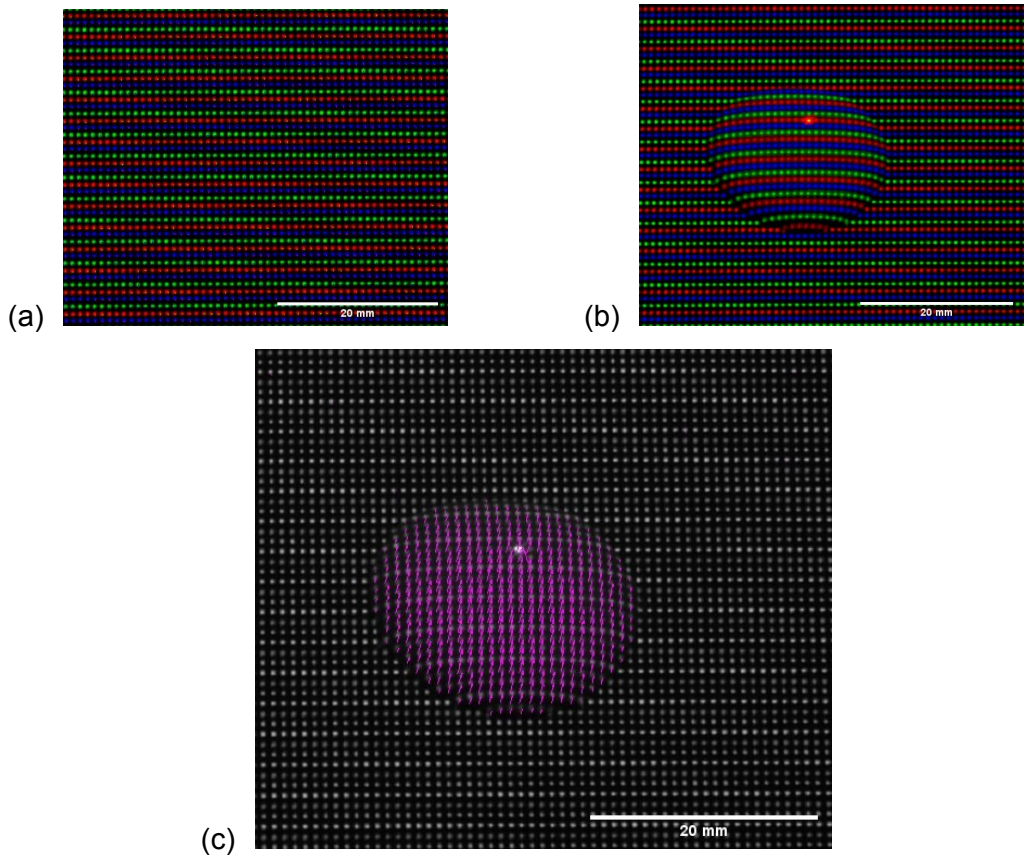

Figure 2-5: A typical result of CCPP method. (a) Reference image, (b) Object image, and (c) Displacement vector field.

The accuracy of displacement measurement is affected by factors like Signal to Noise Ratio (SNR), image contrast, shadows, surface vibration, feature size and orientation, leakage effect due to the camera's sensor, light speckles due to reflection, and the order of sub-pixel polynomial fit. Although it is not practical to completely eliminate all sources of errors, some practices may help to produce a more accurate overall result. Background noise plays a vital role in proper correlation; A noisy image leads to a fictitious thickness profile. One way to eliminate this error is to remove other light sources around the surface under study. Filtering the captured images before processing is another solution. A 3×3 pixels Gaussian filter is chosen here to eliminate random noise in the snapshots before processing. Besides affecting the accuracy, these factors may produce fictitious data, and thus an outlier detection/ correction step is required. This practice is implemented as follows. The two following procedures first categorise the derived vectors into valid and invalid. The first procedure is global, and the vectors are compared with a threshold in terms of value and cross-correlation coefficient. Then, in the second procedure, which is local, each valid vector is compared with its four nearest valid vectors. If the deviation of the centre vector from the average of its neighbourhood is more than three times the standard deviation, it will be considered an invalid vector. Each invalid vector is then corrected by interpolation among its four valid neighbours by using a surface fit. If these points are collinear, the interpolation is impossible. Therefore, the number of involved valid neighbours increases until the interpolation is feasible.

2.1.3 Calibration

All derived data, including the planar size and thickness of the object, is in pixels. Therefore, calibration is required to convert them to real-world dimensions. Although planar calibration is straightforward, thickness calibration needs more effort and equipment. Taking a snapshot of an object with known dimensions and calculating the pixel size is all that is required for planar calibration. For thickness calibration, the effect of thickness must be imitated accurately, which needs a vertical translation stage. The one used for this study is P2XYA from Luminos [Ottawa, Canada], which can expand up to 2.54 mm with 5 μm steps.

The layout of the thickness calibration setup is shown in Figure 2-6. By changing the height of the target with a specific amount and calculating the resultant displacement map, a thickness map is constructed for each elevation change. The overall thickness map is then determined by

fitting a line on the data of each point and finding its slope. Figure 2-7 represents the overall calibration coefficient for a sample point. This chart provides three essential pieces of data. The first is the fit's R-square value, showing a good correlation between the measurements and the linear behaviour assumption made in equation (2-4). It can also be assumed as a figure of accuracy. The second is the slope of the fit, which is used to correlate the displacement map in pixels to thickness map in mm. Thickness measurement range is the last information that is derived from this figure. Before starting the main experiment, we may have some prior knowledge about the maximum thickness of the objects under study. If so, by using this graph, or fit equation, the maximum pixel displacement can be estimated. According to a role of thumb, which says that maximum displacement should be less than half of the point spacing, the proper grid spacing is chosen.

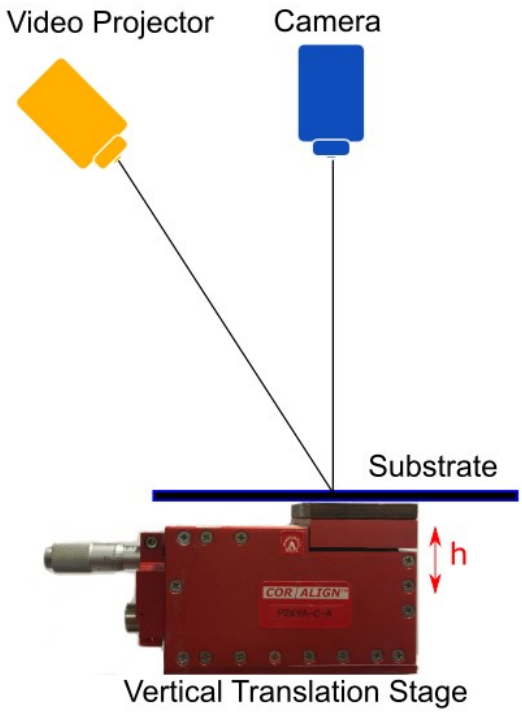

Figure 2-6: The layout of the thickness calibration setup.

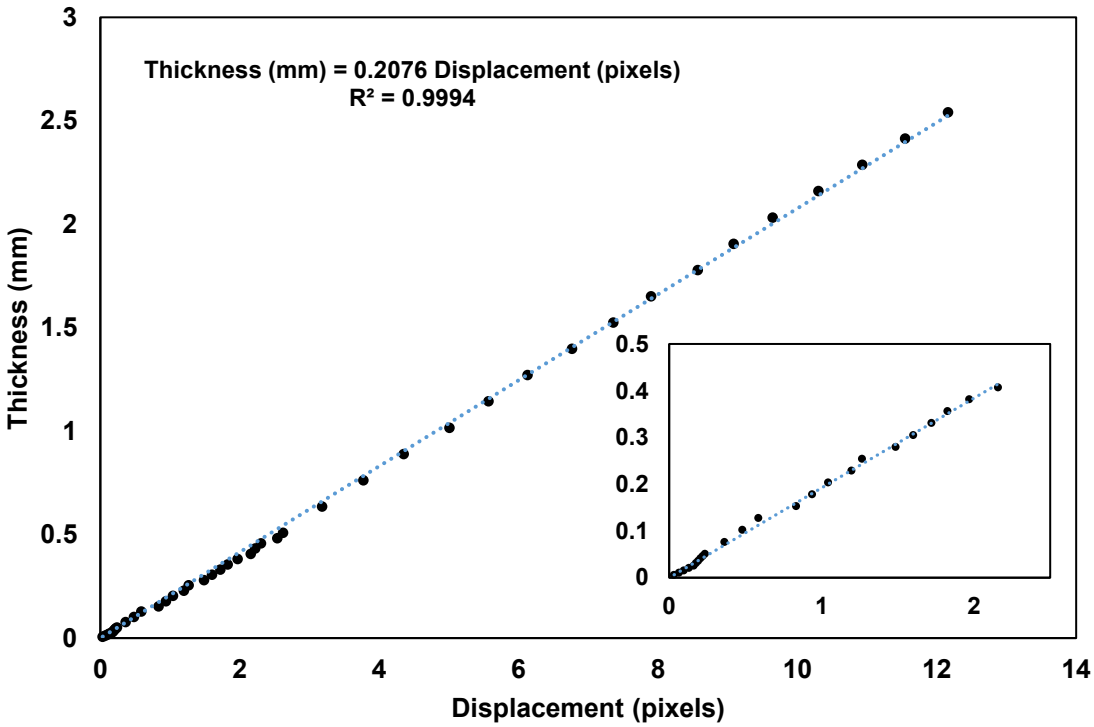

Figure 2-7: The thickness calibration coefficient for a sample point.

2.1.4 Validation

This section provides a validation effort for the proposed method. Figure 2-8 shows a water droplet from three perspectives. Section (a) is the raw image of the proposed method, while sections (b) and (c) show the droplet from the sides, namely from the right and top of section (a) respectively, using the shadowgraphy method. The setup configuration is exactly what was shown in Figure 2-1. While the projection direction is from the bottom of the image shown in section (a), the camera is normal to the substrate. After analysing the captured image and calibrating the setup, the reconstructed profile of the droplet is shown in Figure 2-9. All the units are in mm in this figure, but the scale of the z-axis is independent of the rest. This way of presentation was chosen to show the smooth curvature of the reconstructed droplet, especially at the edges and on the peak.

(a)

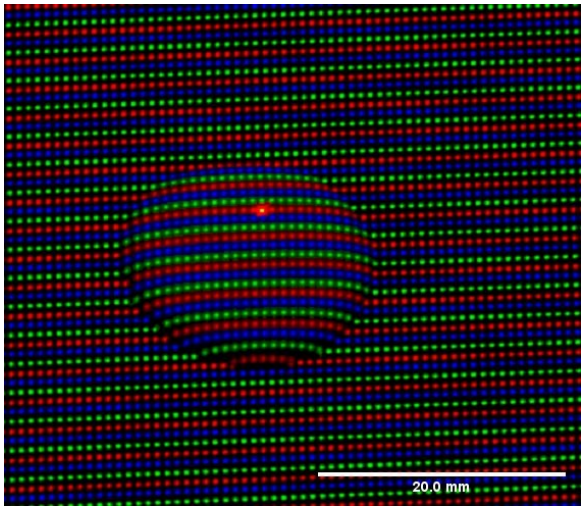

(b)

(c)

Figure 2-8: A water droplet from different views for validation. (a) Top view, (b) Shadowgraphy from the right direction, and (c) Shadowgraphy from the top direction.

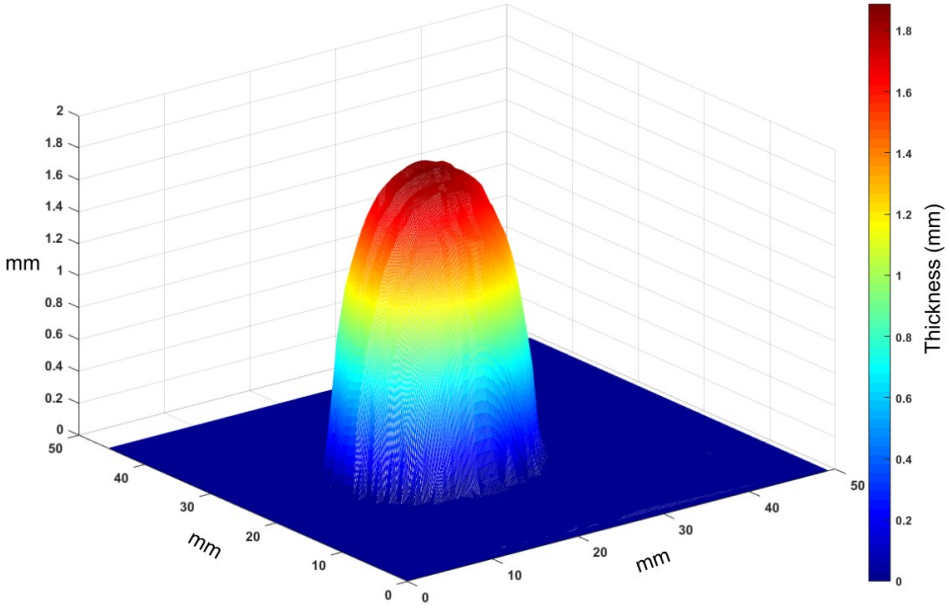

Figure 2-9: Reconstructed droplet.

As shown in Figure 2-10, two slices, crossing the centre of the reconstructed dome, were chosen and compared to the shadowgraphy snapshots, to present the accuracy of the method. The yellow line represents the edge of the droplet, while the red profile is the result of the method. The green line shows the absolute error. The relative error was calculated considering the droplet edge (yellow line) as the reference. Although there is a significant error at the three-phase interfaces, the results around the centre are strongly satisfactory. Statistically, more than 70% of the measurements have less than 5% error. Only in small regions around the three-phase interfaces the error is 60-80%. However, a little bit far from the interfaces the error drops to 20-30%. The overall RMS error is 0.15 mm. It should be noted that not all of the errors are from the proposed method. The unsharp edges in the shadowgraphy images make borders less distinguishable and contribute to the errors. However, the main reasons for the significant error at the interfaces are light penetration and partial points. By using a smarter algorithm, these regions can be detected and then corrected.

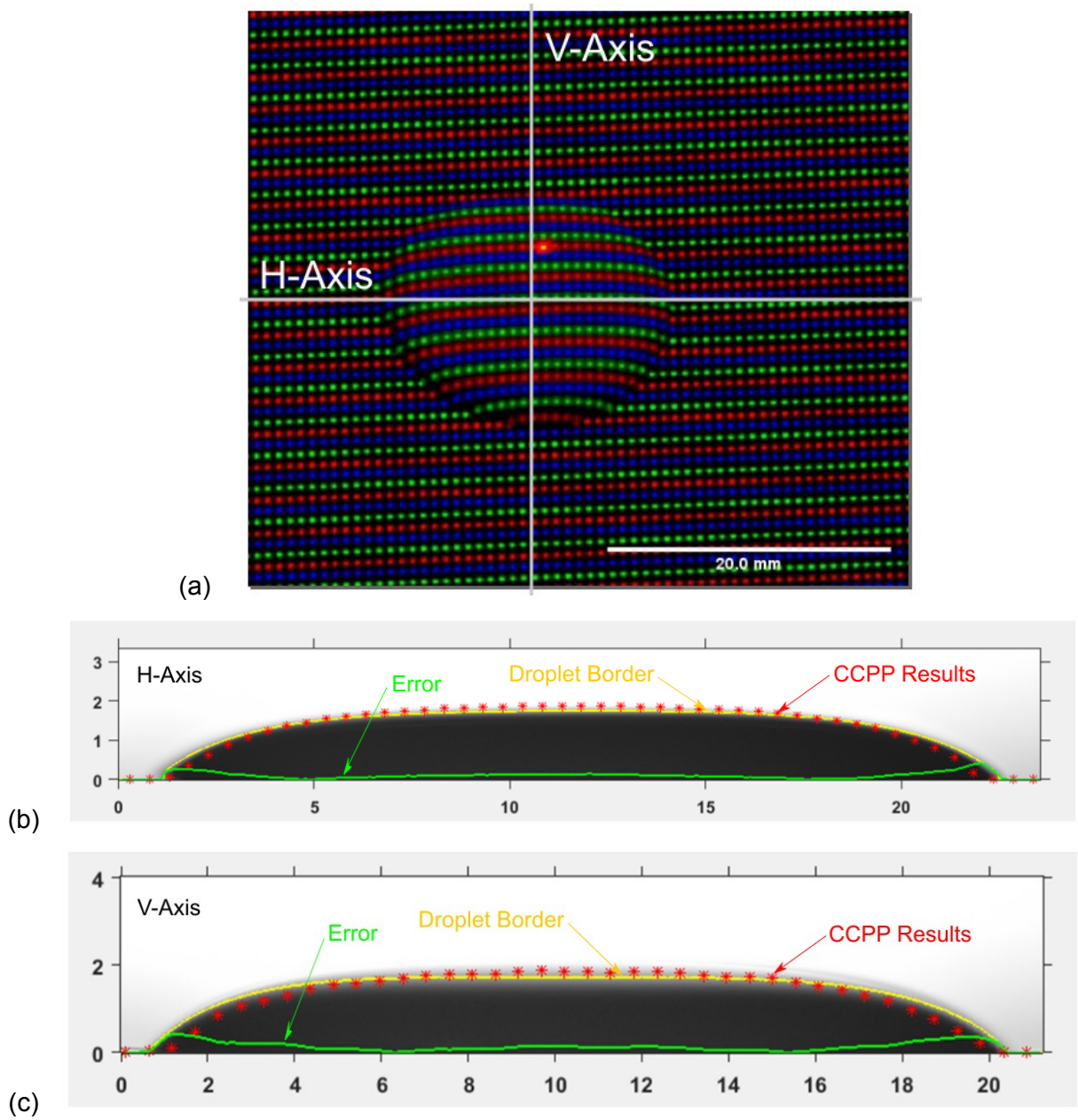

Figure 2-10: Comparison of shadowgraphy snapshots and the estimated curve. (a) Droplet, (b) Horizontal slice, and (c) Vertical slice.

2.2 Experimental Setup

The experiment was carried out inside the icing wind tunnel of Concordia University, which is capable of generating wind speeds up to 90 m/s at the test section and cool it up to -20ºC at sea level. The schematic of this wind tunnel is shown in Figure 2-11 with a short description of each component in Table 2-1. It has an overall dimensions of 22 ft. by 8 ft. The walls are made of

16 gauge stainless steel and insulated with 2 inch polyisocyanurate (32.1 kg/m^3) from Dyplast [Miami, USA]. It has a test section made from acrylic plates with a dimension of 200×200×400 mm (W×H×L). To achieve the desired speed, a 15 hp VJBD-24B6 vane-axial fan from Aerovent [Minneapolis, USA] was used which produces 9000 CFM at 6 in.w.g, at most. An ACH550 drive from ABB [Zurich, Switzerland] controls the fan's motor velocity by changing the frequency in the range of 0-60 Hz. A cross-flow heat exchanger with a capacity of 43000 Btu/h served as the evaporator of the refrigeration system. The condensing unit is an air-cooled type with a capacity of 50,500 Btu/h from Kool-Air Inc. [Delson, Canada], which uses R-404A refrigerant. It was equipped with an internal mixing wide-angle SUJ26B air atomising spray from Spraying Systems [Wheaton, USA] to produce the water mist. Pressure regulators control the spray's water and air pressures, while rotameters monitors the flow rate. The Liquid Water Content (LWC) and droplets Mean Volume Diameter (MVD) are controlled by adjusting the supply pressures. A uniform droplet cloud with a size of MVD = 20 μm at LWC = 5.5 g/cm^3 was produced by adjusting the water and air pressure to 30 psi and 40 psi respectively. The wind tunnel was set to generate two different airspeeds (20 m/s and 40 m/s) at four different temperatures (0^{o}C, -3.5^{o}C, -7^{o}C and -15^{o}C). The camera captures as the spray starts and continues in 3 s intervals. These conditions are summarized in Table 2-2.

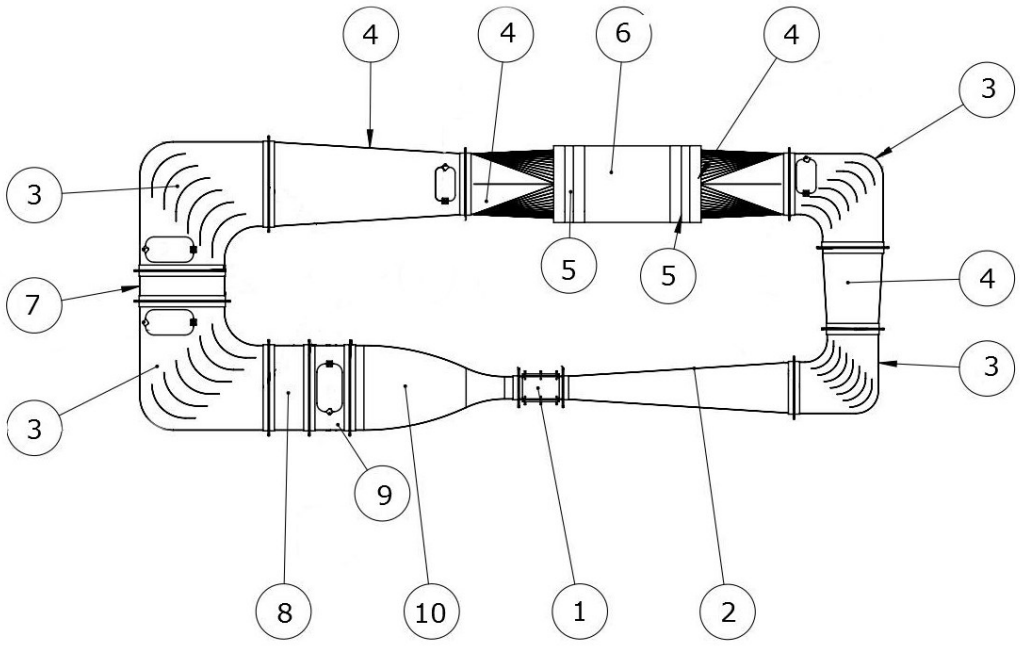

Figure 2-11: Schematic of the icing wind tunnel.

Table 2-1: Wind tunnel components.

Part Number	Description
1	Test Section
2	Diffuser
3	Corner with Guide Vanes
4	Adaptor
5	Flexible Joint
6	Fan
7	Heat Exchanger
8	Settling Chamber
9	Spray Chamber
10	Contraction Section

Table 2-2: Summary of test parameters.

Test No.	V (m/s)	T (^{o}C)	MVD (µm)	LWC (g/cm^{3})	Surface	Test Code
1	20	0	20	5.5	Al	Al/20/0
2	20	-3.5	20	5.5	Al	Al/20/-3.5
3	20	-7	20	5.5	Al	Al/20/-7
4	20	-15	20	5.5	Al	Al/20/-15
5	40	0	20	5.5	Al	Al/40/0
6	40	-3.5	20	5.5	Al	Al/40/-3.5
7	40	-7	20	5.5	Al	Al/40/-7
8	40	-15	20	5.5	Al	Al/40/-15
9	20	0	20	5.5	SH	SH/20/0
10	20	-3.5	20	5.5	SH	SH/20/-3.5
11	20	-7	20	5.5	SH	SH/20/-7

A NACA 0012 airfoil with 10 cm span and 10 cm chord, as depicted in Figure 2-12, is used to imitate the wing. It has a 6 mm thick acrylic structure covered by 6061 aluminium sheet with 0.4 mm thickness. The airfoil is installed inside the wind tunnel at 0^o angle of attack. The experiment is done twice to compare the effect of the surface on the ice accretion, once with bare aluminium and again on a superhydrophobic surface. The superhydrophobic condition is provided by coating the airfoil with WX2100 spray from Cytonix [Beltsville, USA], which provides a contact angle of over 150^o. Three layers of the coating were applied on the clean and dry aluminium surface with 2 hours interval between each spray. The surface then was kept dry to cure completely and was used in experiments after 24 hours.

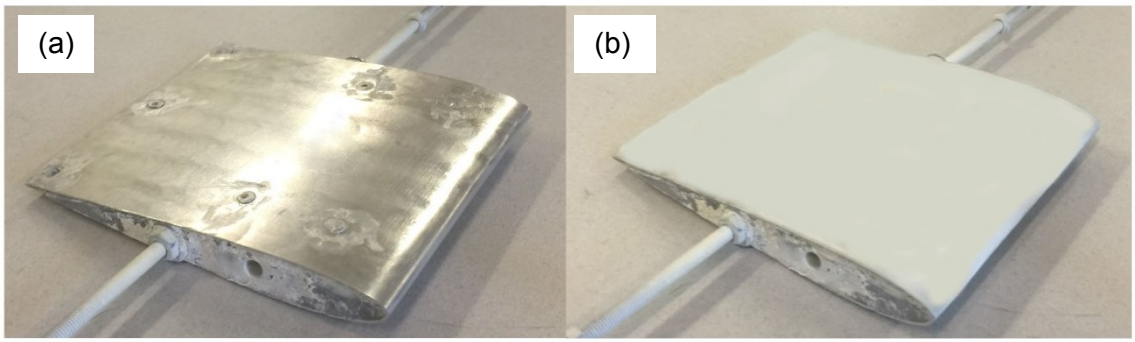

Figure 2-12: NACA 0012 airfoil. (a) Uncoated surface, and (b) Superhydrophobic coated surface

The experimental setup is shown in Figure 2-13, consisting of a projector at a small angle from the vertical direction and a camera looking downward to the airfoil. Since the camera is normal to the airfoil chord plane, no camera calibration is required. The projector and camera were installed along the span-wise direction (normal to the flow direction) to avoid light speckles, especially from the leading edge. The average vertical distance between the surface and the camera and projector was about 40 cm, while the horizontal distance between them was 15 cm. The projector is a DELL DLP (1650) projector with a resolution of 1280×800 pixels, and the zoom level was adjusted to the minimum level to have the finest pattern. The brightness and contrast levels were adjusted, by trial and error, to 20 and 50 respectively to provide better images. The camera is a Nikon DSLR (D90) camera with the resolution of 2144×1424 pixels attached to a Nikon AF NIKKOR 50 mm f/1.8D lens set to f/22 aperture. All images were taken in the manual mode with ISO 200, a shutter speed of 1/100s, and aperture of f/50. The side view images for validation were captured with a Nikon AF-S Micro NIKKOR 105mm f/2.8 lens. Before each

experiment, the focus of the projector and camera were adjusted precisely to have the sharpest images.

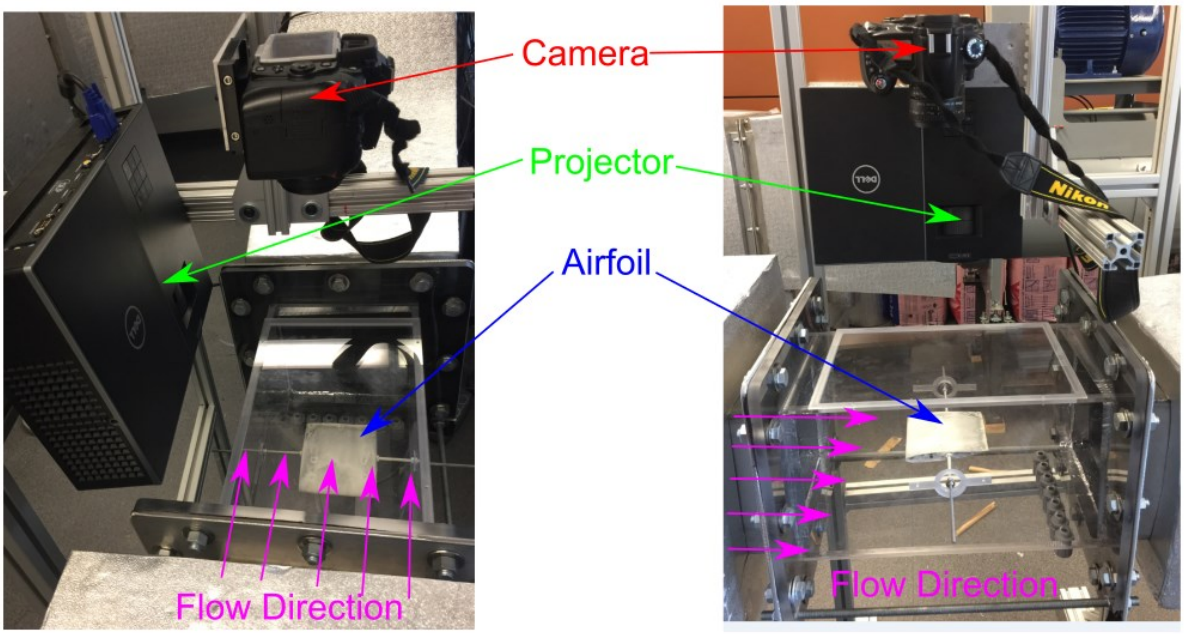

Figure 2-13: Experimental setup.

The colour-coded point pattern is shown in Figure 2-14. It consists of individual pixels in three colours (red, green, and blue). The implemented colour-coding scheme has the colour change just in one direction, which is parallel to the projector-camera axis. Because of high light reflections from the surface and a leakage problem due to the camera's sensor, it was found that this 4×4 pattern was the minimum distinguishable size. The source of this limitation is either the projector or the camera. Projecting finer dots which also have enough intensity is the solution for the projector side. More resolution and more colour sensitivity also eliminate camera-related problems. As explained before, another issue that limits the grid size is the thickness measurement range. Table 2-3 shows the experimentally derived information for the current configuration. It shows the required grid spacing for a specific thickness measurement range and the resultant planar resolution. It is clear that there is a trade-off between the measurement range and planar resolution and, therefore, the grid spacing should be set according to the approximate size of the object under study. Although the vertical spacing (according to Figure 2-14) has a limitation according to Table 2-3, horizontal spacing may have any value as long as it is more than the minimum

distinguishable value. This feature may help to produce a finer planar resolution in large object measurements. Throughout the experiments in this thesis, a 6×6 grid spacing was used.

Table 2-3: Measurement range as a function of grid size.

Grid Spacing (pixels)	Thickness Measurement Range (mm)	Planar Resolution (mm)
4	0.91	0.70
6	3.90	1.05
8	6.89	1.40
10	9.88	1.75
12	12.87	2.10
14	15.86	2.45
16	18.85	2.80
18	21.83	3.15
20	24.82	3.50

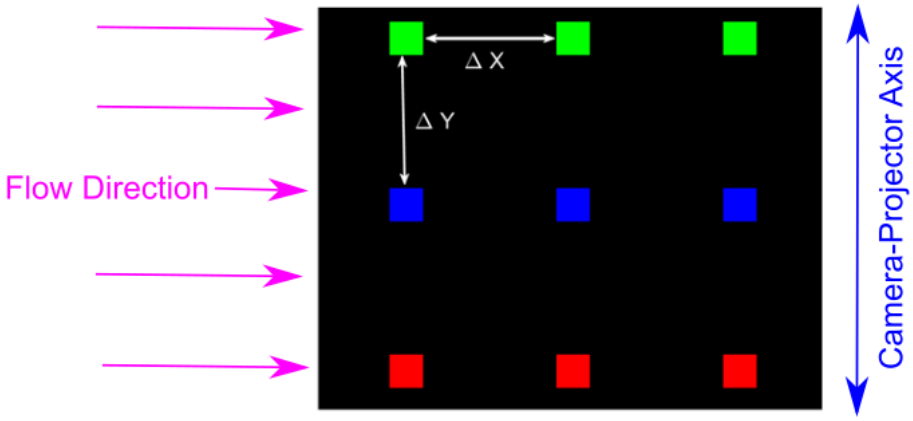

Figure 2-14: The colour-coded point pattern.

Because this method extracts data from the deformation of a pattern projected on the surface, the optical properties of the object under study are essential. In other words, the surface must scatter the light. Due to diffusion, the light rays enter the water about 4-5 mm before reflection, which is not desirable for the study of small phenomena. Adding some additives to the water can rectify this transparency problem. These additives must enhance the water surface

reflectance and not change the physical properties of the water, like density and surface tension. Different materials like acrylic paint [43] and white liquid dye [29] were reported in the literature. However, this added impurity affects the behaviour of the film by changing the water's physical properties. Przadka et al. [49] showed that by using anatase (TiO_2) pigment, this problem would be avoided. He reported that the optimum pigment concentration is 2 g/l of Titania with a particle size of 300 nm. He claimed that the surface tension of this aqueous suspension is 70 mN/m, while the value for pure water is 71 mN/m. For this study, a small amount (less than 2% volumetric) of a high glossy titanium white acrylic pigment (PW 6) was added to the water.

3 Results and Discussions

In this chapter, the utilisation of the proposed method is investigated. The results are divided into two main parts: (1) method characterisation and (2) wind tunnel investigation. In the first part, the requirements for image quality are defined, and then the effect of light penetration is discussed. The second part is devoted to proving the feasibility of using this method in real wind tunnel experiments. The results shown here are typical and show the ability of this method to measure ice thickness during formation. A comprehensive study consisting of repeated experiments under well-controlled conditions is required to investigate the effect of different parameters like temperature, velocity, and surface on ice formation, which is left as future work.

3.1 Method Characterization

Every measurement method must be assessed at first to prove its capabilities and limitations for specific experimental conditions. This section first investigates the minimum image quality required for the proposed method to work successfully and then peruses the amount of error involved in shifting from measurement of solid objects to the case of liquids.

3.1.1 Image Quality Requirements

As with other optical methods, the quality of the captured images is the most crucial issue. Speckles due to reflection, light penetration, light attenuation, surrounding light disturbance, and the camera's sensor saturation reduce the image quality and produce an erroneous result. Because

of these problems, a test was done to find the minimum required image quality. In this test, the calibration setup was used and the elevation was set to a specific amount. The displacement map is available entirely from the calibration step. The image quality can be characterised by the intensity (contrast) of features in the captured image relative to the background. The intensity of the projected points was reduced in 20 steps to imitate the reduction in image quality. Then the displacement map was calculated at each step.

The standard quantity for comparing the quality of images is Signal to Noise Ratio (SNR). Because all the data come from the displacement of the points, it is deduced that an image without any point is all noise and its difference from an image with points is signal. Therefore, the SNR is formulated as

$$SNR = \frac{\mu(I - I_0)}{\sigma(I_0)} \tag{3-1}$$

where I_0 is the image without any points (zero intensity) and I is the image with points (non-zero intensity). μ and σ are the operators for average and standard deviation, respectively.

Two criteria were defined to assess the ability of the method at different image quality. The first one is code failure, which is the ratio of the points with invalid data to their total number. The other one is the normal distribution test and relies on the normal distribution fit of data from the image with the highest intensity. All measurements at other image qualities which are not in the six-sigma region of this distribution are invalid. As show in Figure 3-1, the six-sigma region is where 99.7% of the data can be assumed valid.

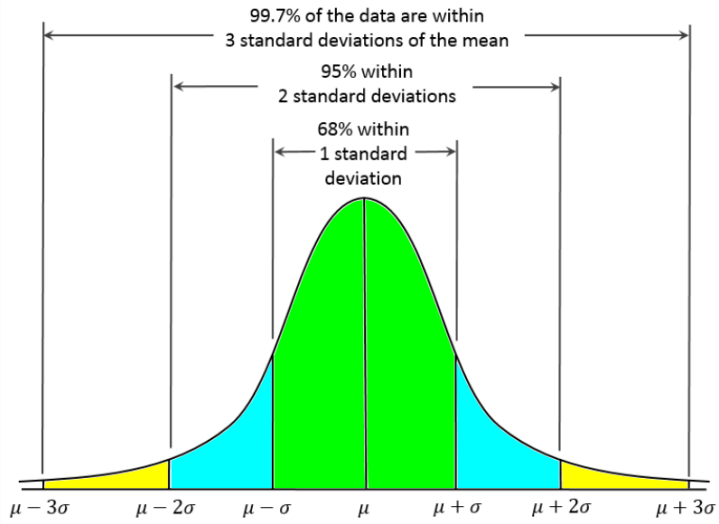

Figure 3-1: Normal distribution.

Figure 3-2 shows the results of these two criteria as a function of SNR. At lower values of SNR, when the order of the signal and the noise are almost the same, both criteria fail. By increasing the SNR, the level of contamination of the data by noise is decreased, and hence, the method provides more valid data. The SNR should be at least four to have valid data. Although these criteria calculate the failure in two different way, there is a good correlation between them. This correlation shows that all valid data are consistent and, therefore, likely to be accurate.

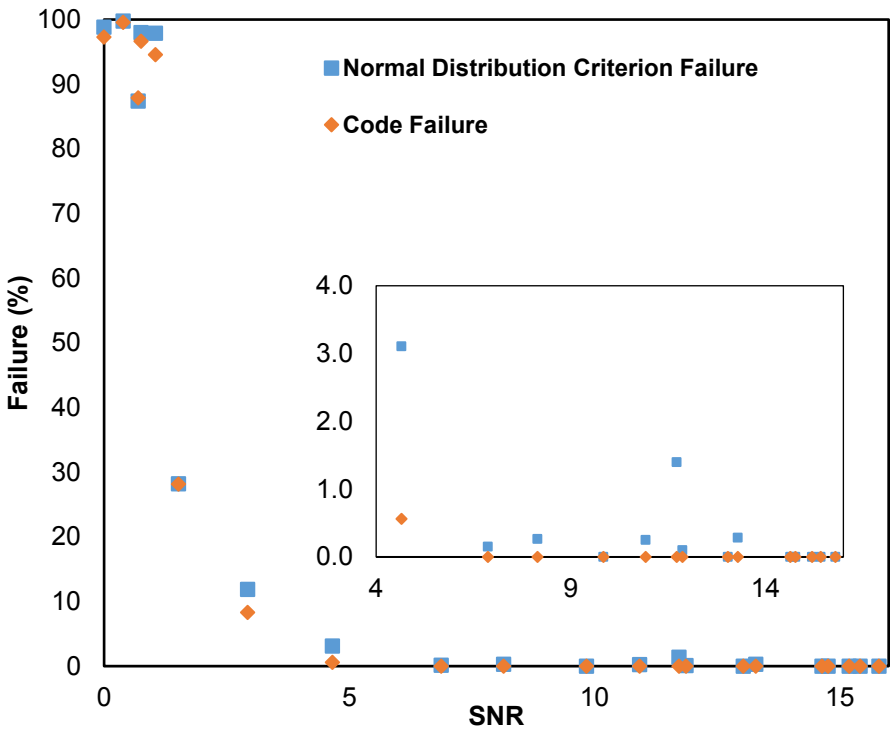

Figure 3-2: SNR requirements.

3.1.2 Light Penetration Characterization

The proposed method is based on the reflection of light from the object's surface. Therefore, the ideal case would be a perfect light reflection without any penetration. Although water is contaminated by colour to improve the opacity, what happens, in reality, is entirely different. There is always some light penetration, which is a source of error. As depicted in Figure 2-10, although there is a good match on top of the droplet, some deviations are apparent at the sides, where the thickness of the liquid is less. Thus, to have a better idea of the accuracy of the method, the sensitivity of this method to light penetration should first be characterised.

The characterisation setup consists of two transparent thin glass sheets and a micrometre, as shown in Figure 3-3. The glass sheets were attached to the micrometre, and the space between them was filled with coloured water. Since the thickness of the liquid layer is small, the water remains between the glass sheets. The lower glass sheet was painted in white to be completely opaque. Although the upper sheet is thin, it introduces a shift about 3 pixels due to the light refraction inside it. Since this shift is present in both the reference image and object image, it is

cancelled out in point displacement calculation. Therefore, it can be assumed that all reflections were from the water surface. The liquid film thickness can be imitated by changing the distance between the sheets. Therefore, the effect of light penetration was studied by comparing the results with calibration data, which was assumed as a reference.

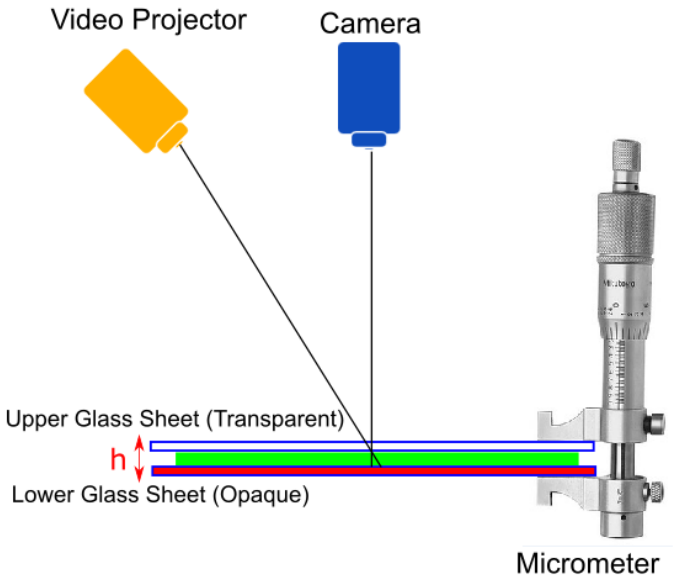

Figure 3-3: Test setup for light penetration characterisation.

The measurements of both solid and liquid surface are compared in Figure 3-4. Although both measurements have a good match with a linear fit, the fit on the liquid surface has an intercept value. This intercept means that small film thicknesses cannot be measured by this equipment. On the same physical thickness, the measured displacements on a solid surface are more than on liquids. This means that the thickness measurement is always underestimated in the case of a liquid. In addition, the deviations between the solid and liquid measurements increase when the film thickness decreases. These show the effect of light penetration clearly.

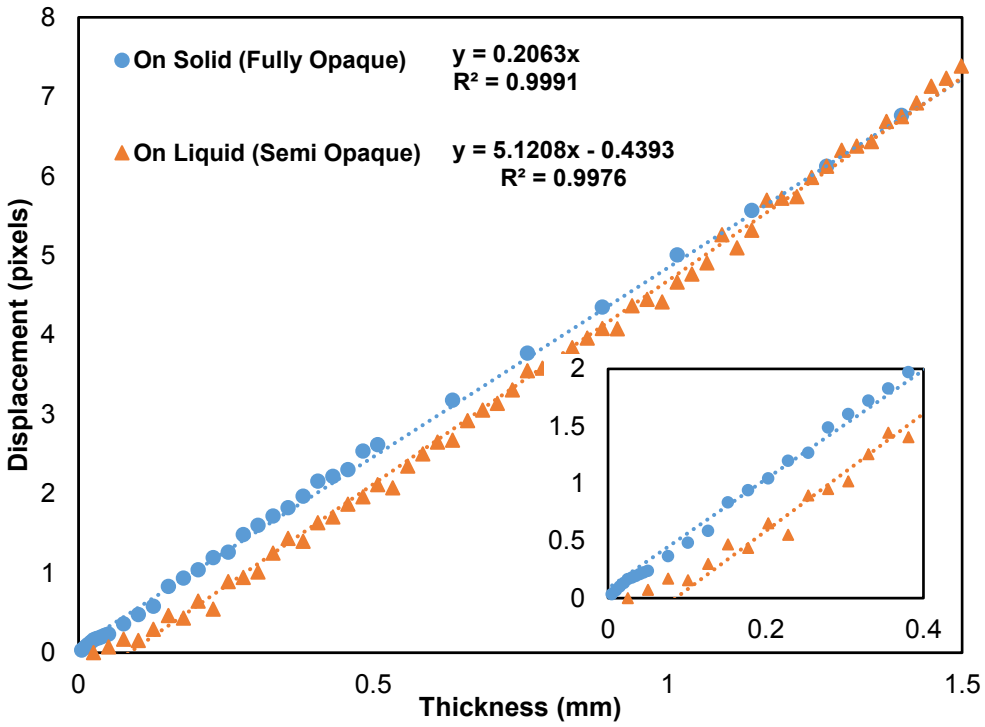

Figure 3-4: Light penetration characterisation.

The behaviour on the liquid surface is quantised in Figure 3-5. The relative error was calculated by assuming the solid measurements as a reference. The experiment shows that the thickness measurement of liquid surfaces less than 600 microns has an error of more than 10%. Another defined criterion is uncertainty, which is the ratio of the numbers of points with invalid measurement to the total number of points. It can be deduced that, for film thicknesses more than 50 microns, all measurements are valid. Most of the invalid data can be corrected subsequently by considering valid neighbours. However, when the uncertainty exceeds 50%, meaning the invalid data are more numerous than valid ones, the correction will be impossible. Therefore, the practical smallest measurable thickness is about 50 microns, regardless of errors due to light penetration.

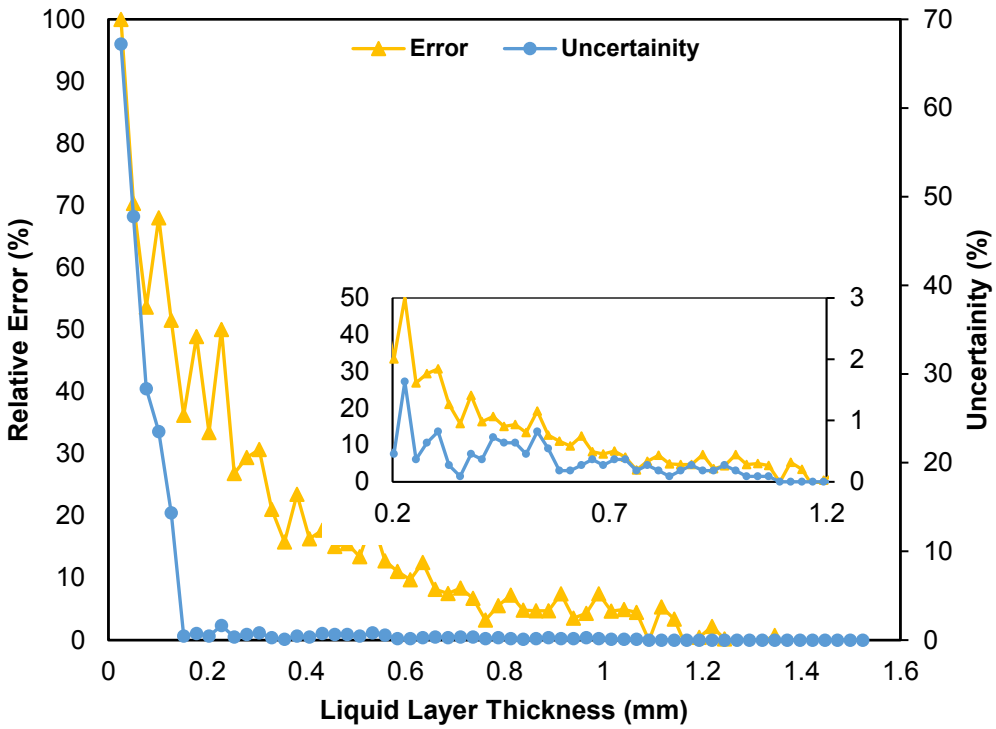

Figure 3-5: Quantization of light penetration.

3.2 Wind Tunnel Investigation

The capability of the proposed method to measure liquid objects was proved so far. Now the goal is to test it in real wind tunnel experiments. The experiment parameters and conditions were shown in Table 2-2. Different quantities and results can be extracted from the thickness profile, depending on the goal of the experiment. This section provides some extractable quantities and then investigates the effect of each parameter on the behaviour of the phenomena. The scope of view is from some point near the leading edge (X/C~ 0.03) to the trailing edge, due to the curvature of the airfoil and the camera's orientation limitation. Therefore, some data around the leading edge is missed. Moreover, there is no surface in the upstream region of the leading edge. Thus, finding reference points in this region (from the first image) is impossible. Consequently, the study of ice formation on the leading edge and its growth in the opposite direction of the air stream is not feasible. Furthermore, there is no way to distinguish between ice and water, and hence, the measured values are thicknesses of both.

3.2.1 Thickness Profile Visualization

A visual presentation helps us to compare the measurement with what is on the airfoil. This visualisation is provided in Figure 3-6 to Figure 3-8. The chord-wise and span-wise directions were normalised by the airfoil's dimensions and the thickness profile is in mm. Figure 3-6 shows the formation of rivulets for Al/20/0 at t= 6 s. At T= 0^{o}C, the force of surface adhesion is less than the drag force. Therefore, the nucleation sites at the rivulets' heads are still moving. Although the film at the leading edge was not captured completely, the separated rivulets are distinguishable in the reconstructed profile. The experiment for Al/20/-3.5 is shown in Figure 3-7 at t= 30 s. the ice formation around the leading edge and then forming the continuous rivulets were captured successfully. In the same way, Figure 3-8 represents the formation of ice, likely rime ice, at the leading edge of the airfoil for Al/20/-3.5 at t= 30 s. In this condition, all the water freeze at the impact location and, therefore, no rivulets form at downstream. These results prove the method's capability for capturing different phenomena in wind tunnel experiments.

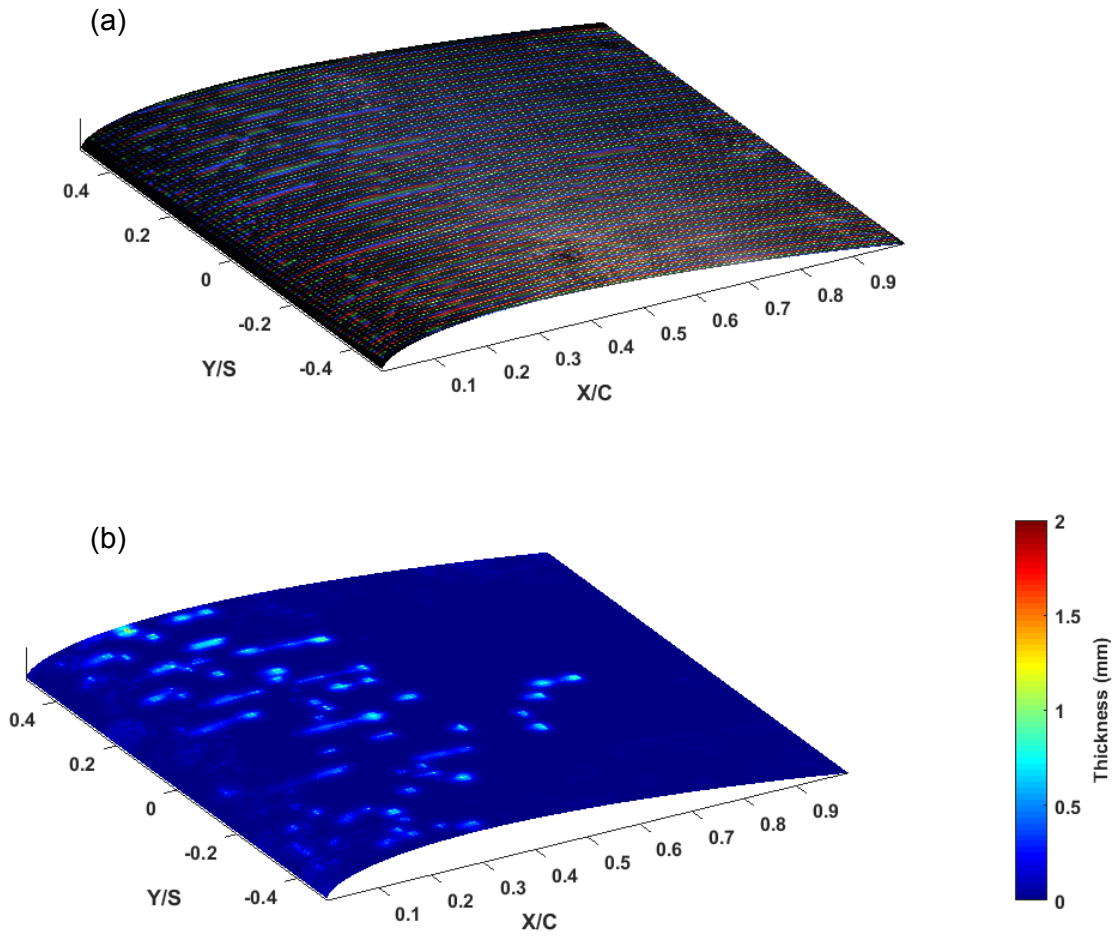

Figure 3-6: Water/ ice thickness profile for Al/20/0 at t= 6s, (a) raw image and (b) reconstructed profile.

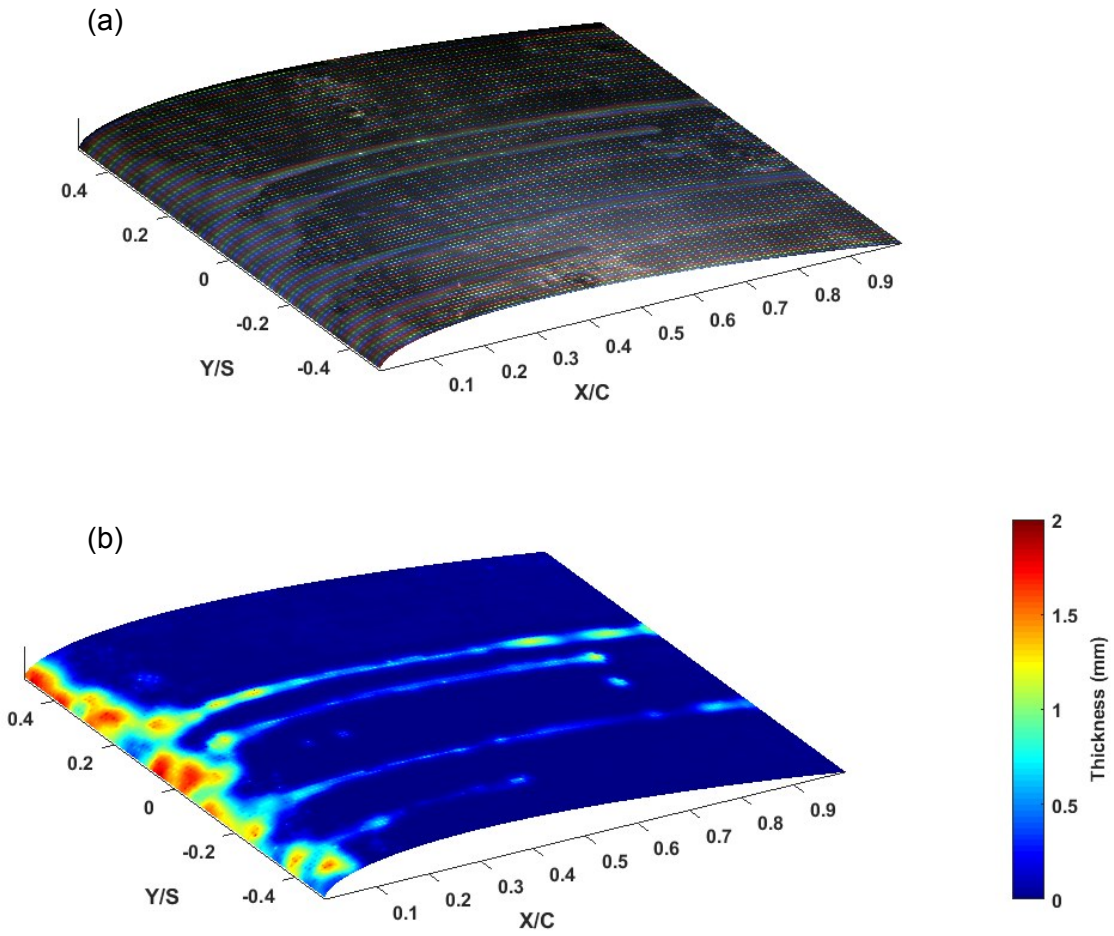

Figure 3-7: Water/ ice thickness profile for Al/20/-3.5 at t= 30s, (a) raw data and (b) reconstructed profile.

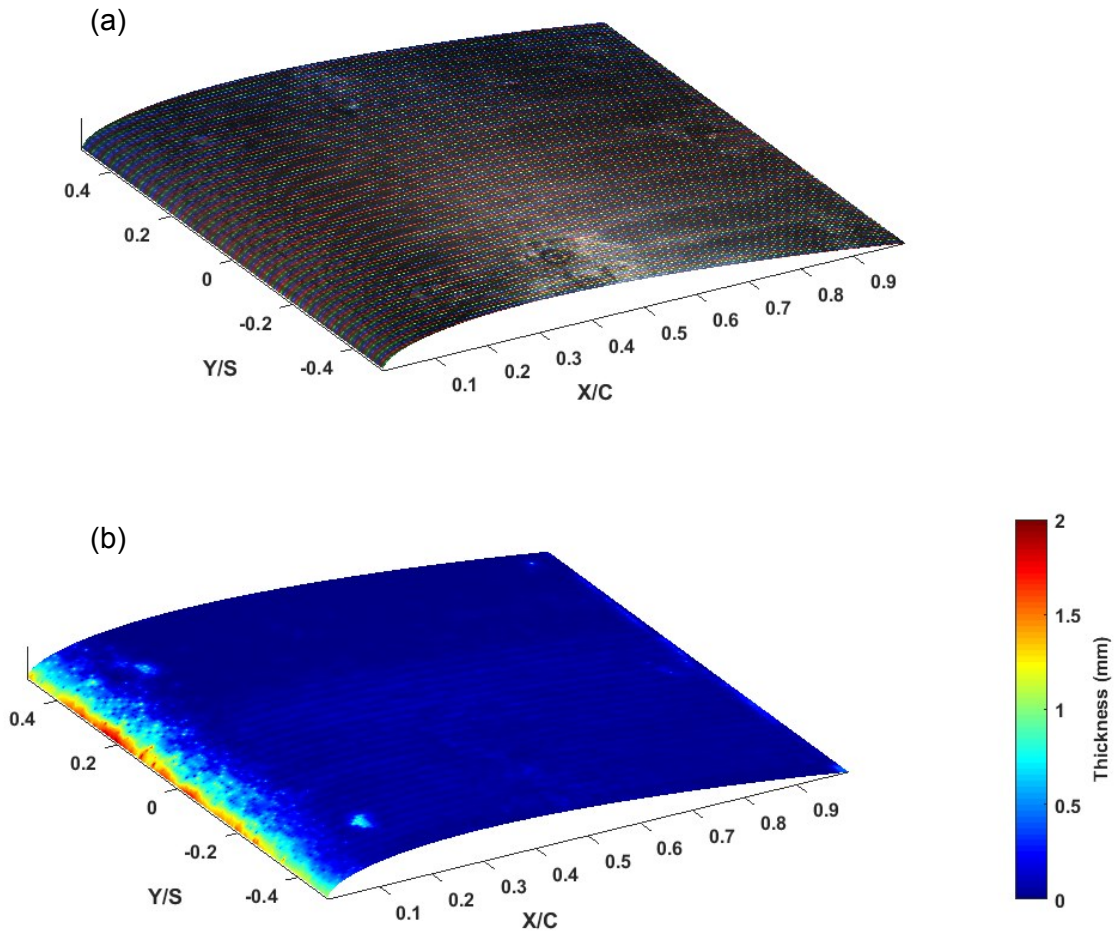

Figure 3-8: Water/ ice thickness profile for Al/20/-15 at t= 30s, (a) raw data and (b) reconstructed profile.

3.2.2 Rivulet Study

The flow at temperatures near or higher than the freezing point is in the liquid phase. Therefore, the liquid film is formed first at the leading edge. After a specific location that depends mainly on the speed, rivulets are formed. Assuming that, after passing a small amount of time, the flow reaches a semi-steady condition, which means that there is no new rivulet after this time, and they act like channels in which water is passing along the airfoil. The formed rivulets/film on three experiments with different velocities and surfaces at t= 18 s are shown in Figure 3-9. To eliminate the side effects on the span-wise direction and random behaviour of the phenomena, the Region Of Interest (ROI) was defined with the width of 20% of the span around the airfoil's centreline, as shown in Figure 3-10.

(a)

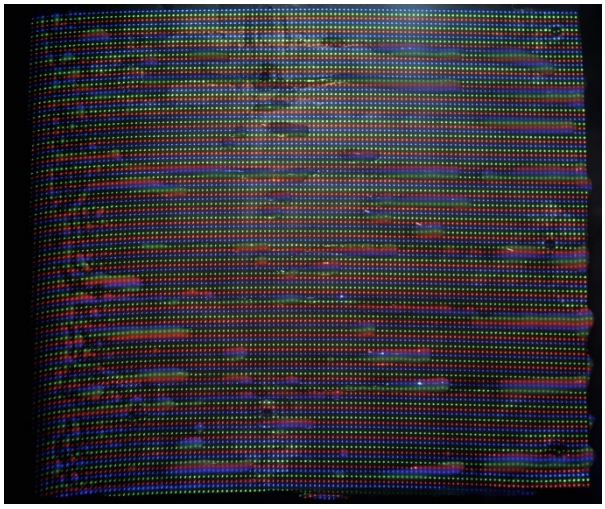

(b)

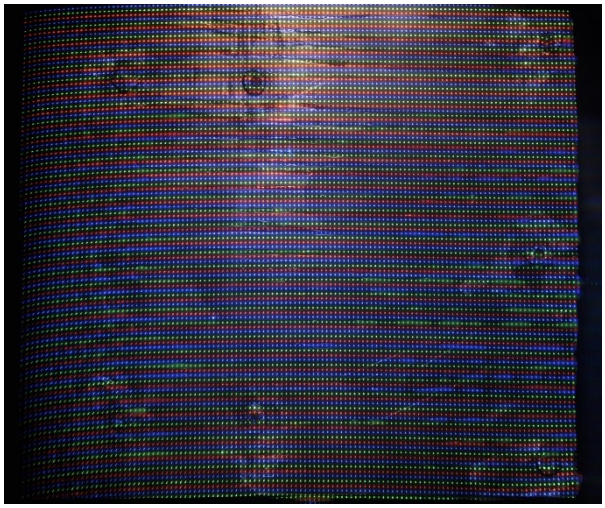

(c)

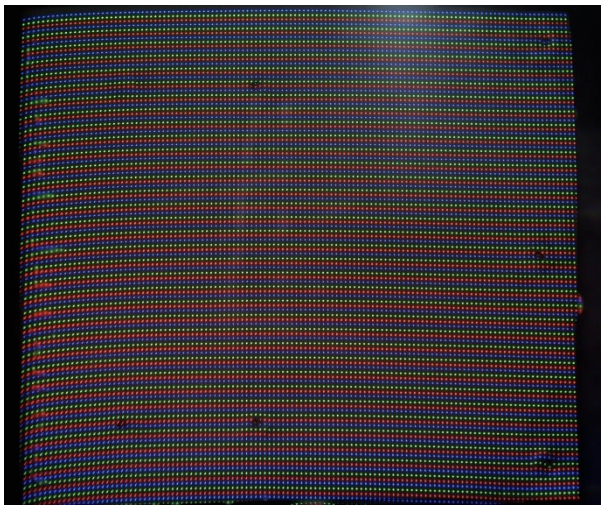

Figure 3-9: Rivulet and film formed in different experiments at t= 18s. (a) Al/20/0, (b) Al/40/0, and (c) SH/20/0.

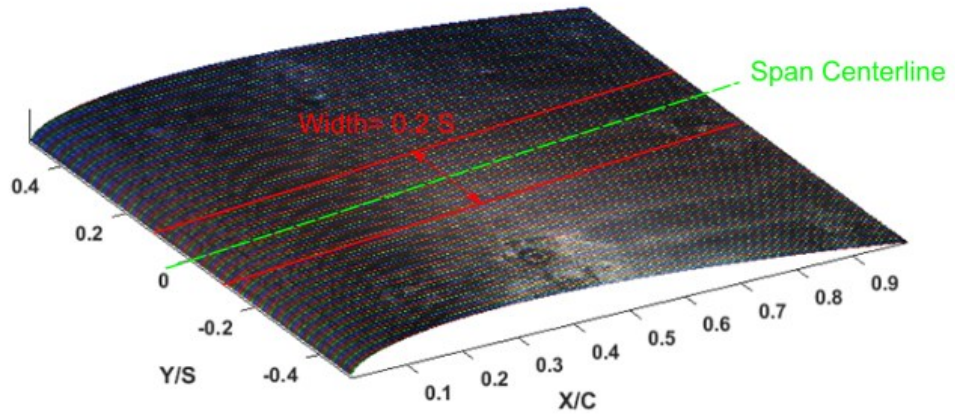

Figure 3-10: Definition of the Region Of Interest (ROI).

Knowing the range of the rivulet/film thickness is helpful. Figure 3-11 shows the frequency chart of these values in bins with 50 µm width at t= 18 s in the ROI. The reported thickness values are rivulets and film, all together. Assuming that the measurement sensitivity is 50 µm, the values in the first bin are either accurate measurements smaller than 50 µm or noise, and the rest are accurate. The proportion of acceptable values for Al/20/0, Al/40/0, and SH/20/0 are 66%, 36%, and 50%, respectively. Because of this issue, comparing the thickness distribution is impossible in this situation. As an alternative quantity, the range of measured thickness can provide a clearer picture for comparison. The median thicknesses for Al/20/0, Al/40/0, and SH/20/0 are approximately 275 µm, 150 µm, and 75 µm, respectively. This means rivulets on the superhydrophobic surface are thinner than on aluminium. Assuming the same mass flow rate, the film and rivulets on the superhydrophobic surface are moving at a faster velocity and thus have less contact with the surface. By increasing the velocity, both the thickness and the size of rivulets are decreased. In general, the accuracy of the measurements is not high enough to provide an acceptable thickness profile for the rivulets or film.

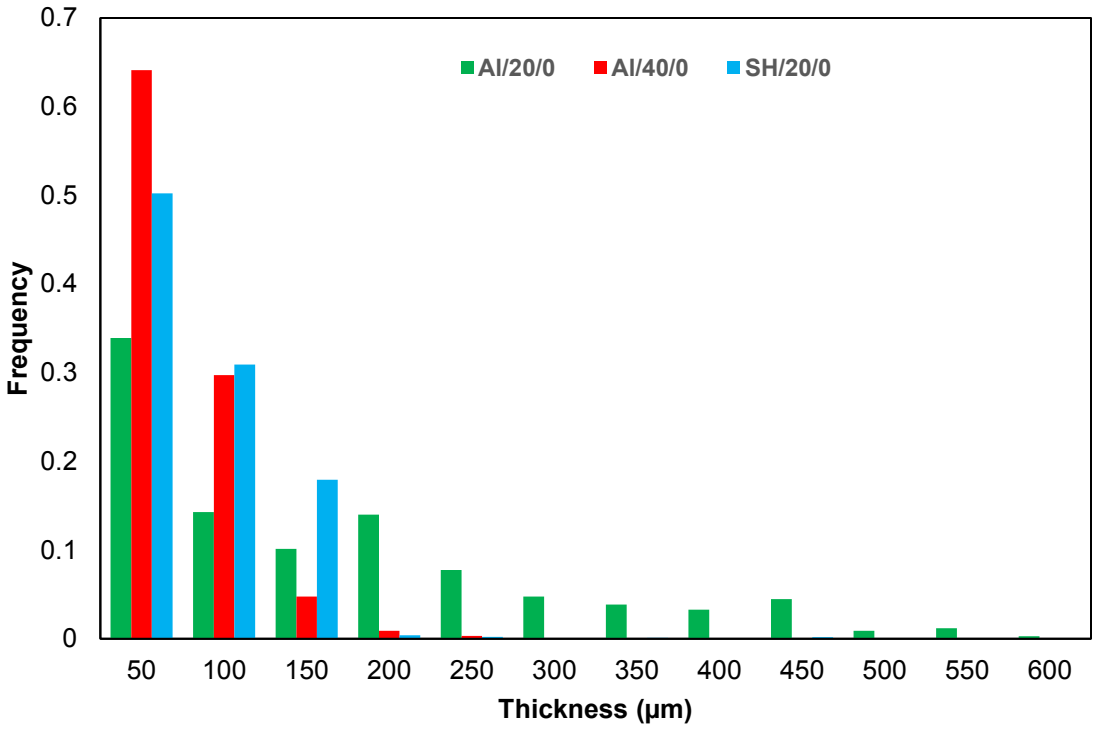

Figure 3-11: Frequency of the thickness distribution of rivulets/film.

3.2.3 Temporal Variation

Study of the dynamic ice formation by time reveals various information regarding the location and overall shape of the ice on the scope of view. Raw images of the aluminium surface with an airflow with the speed of 20 m/s at different temperatures are shown in Figure 3-12. The corresponding results for a span-wise average of the ROI are shown in Figure 3-13 to Figure 3-15. Ice accretion far from the impingement area in Figure 3-13 confirms the formation of a runback in Al/20/-3.5, while most of the ice is concentrated on the leading edge at the lower temperature (Figure 3-14). By decreasing the temperature, the type of ice is changed from glaze to rime. This fact can be deduced from Figure 3-15 by considering very little ice accumulation on the downstream of the leading edge (between X/C= 0.03 to X/C= 0.2). Raw images confirm these results. It should be noted that this method only covers a location downstream of the leading edge (X/C~ 0.03) to the trailing edge, as explained before in section 3.2.

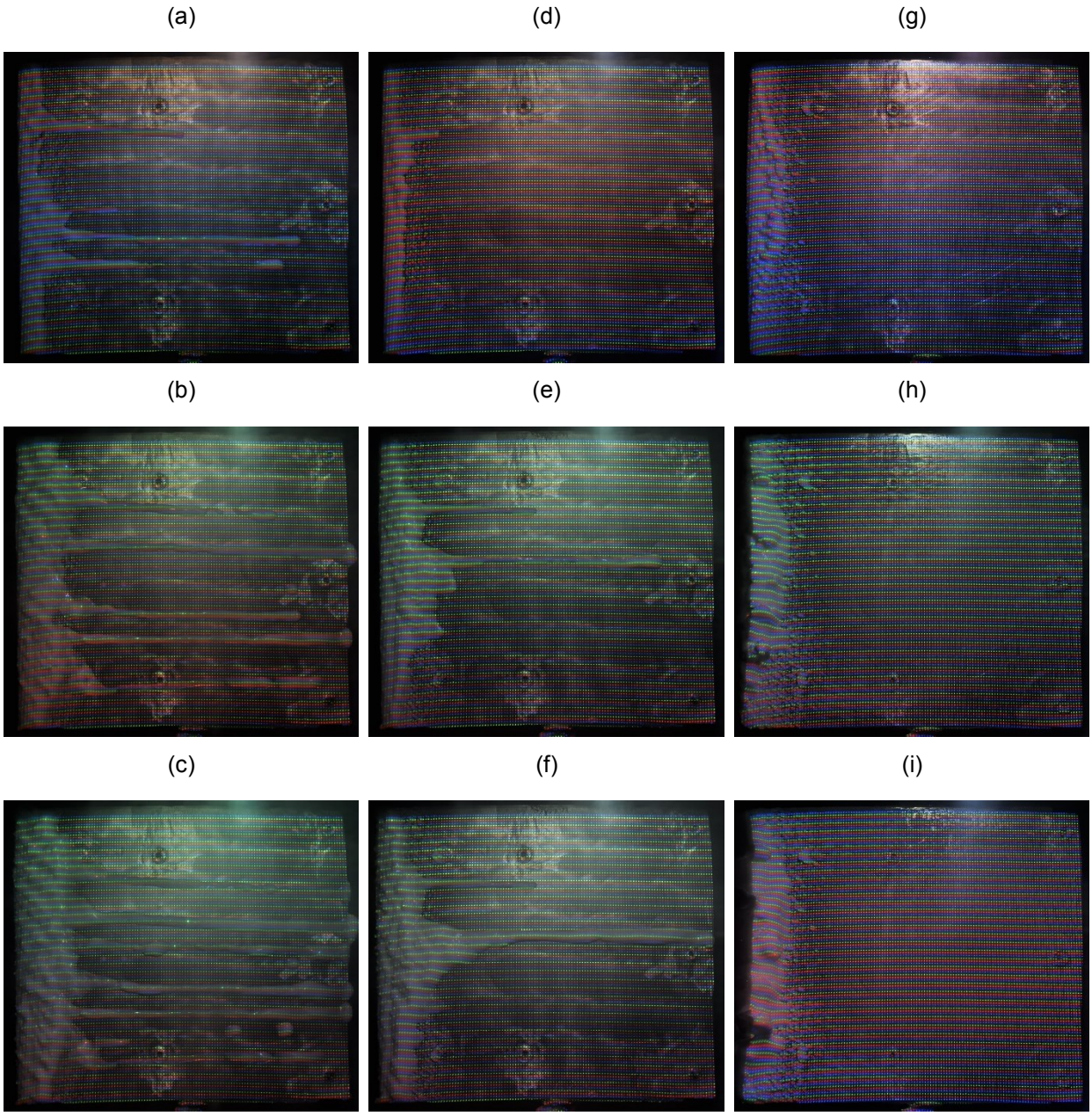

Figure 3-12: Raw images. From top to bottom, t= 0 s, t= 15 s and t= 45 s. (a-c) for Al/20/-3.5, (d-f) for Al/20/-7, and (g-i) for Al/20/-15.

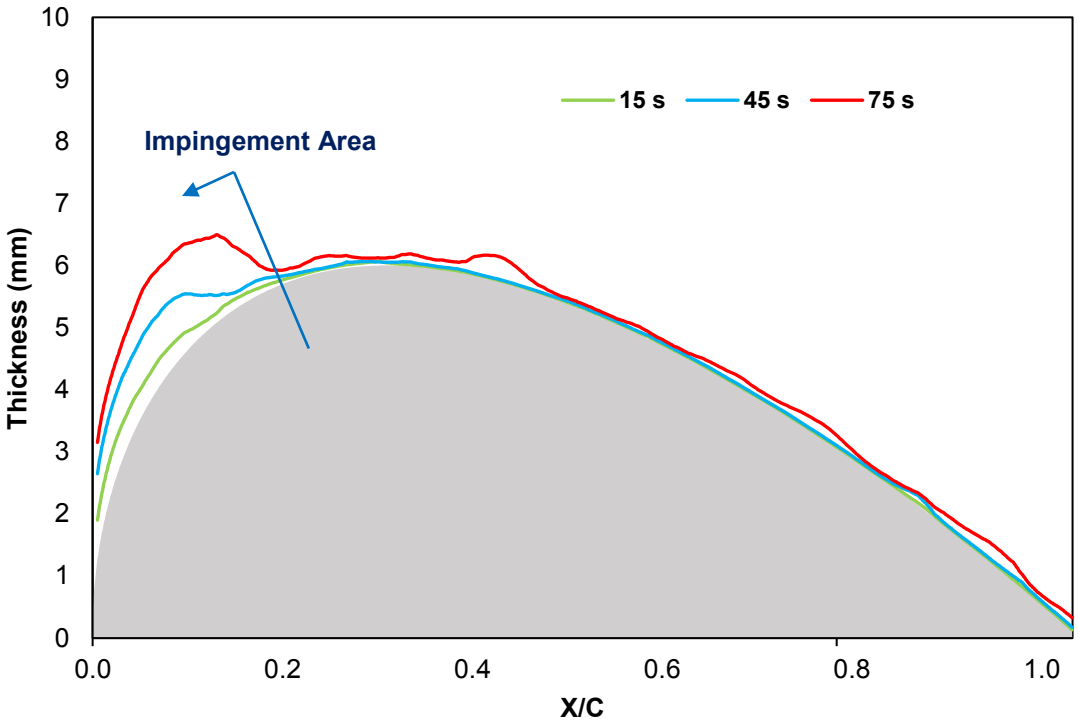

Figure 3-13: Ice/water thickness evolution by time for Al/20/-3.5.

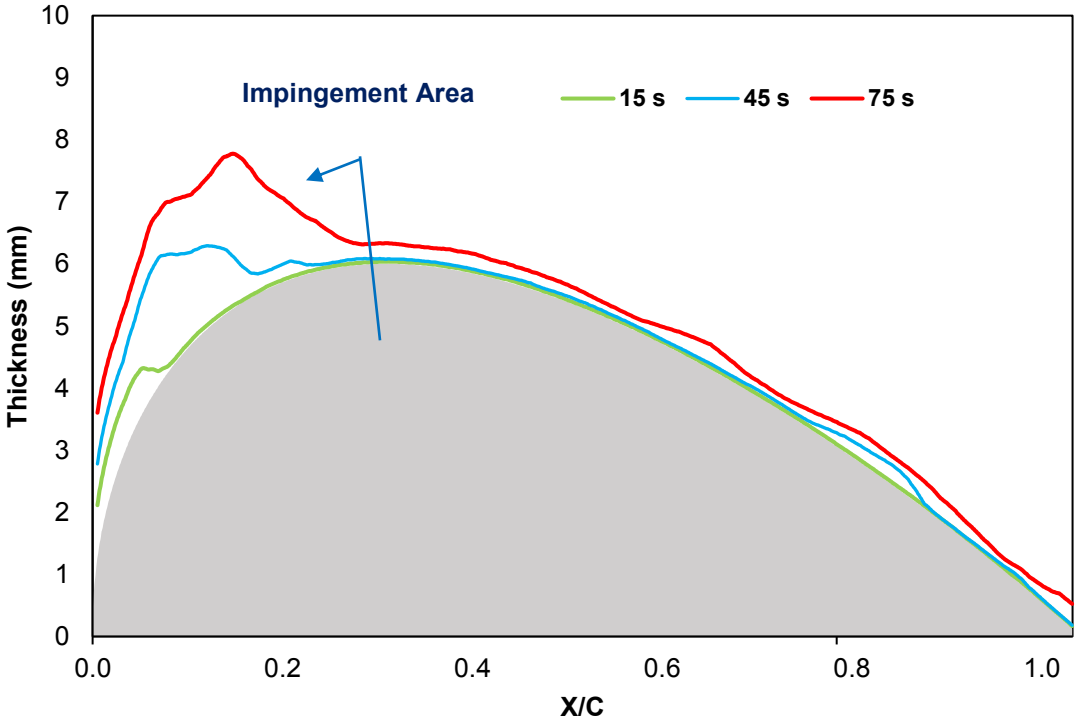

Figure 3-14: Ice/water thickness evolution by time for Al/20/-7.

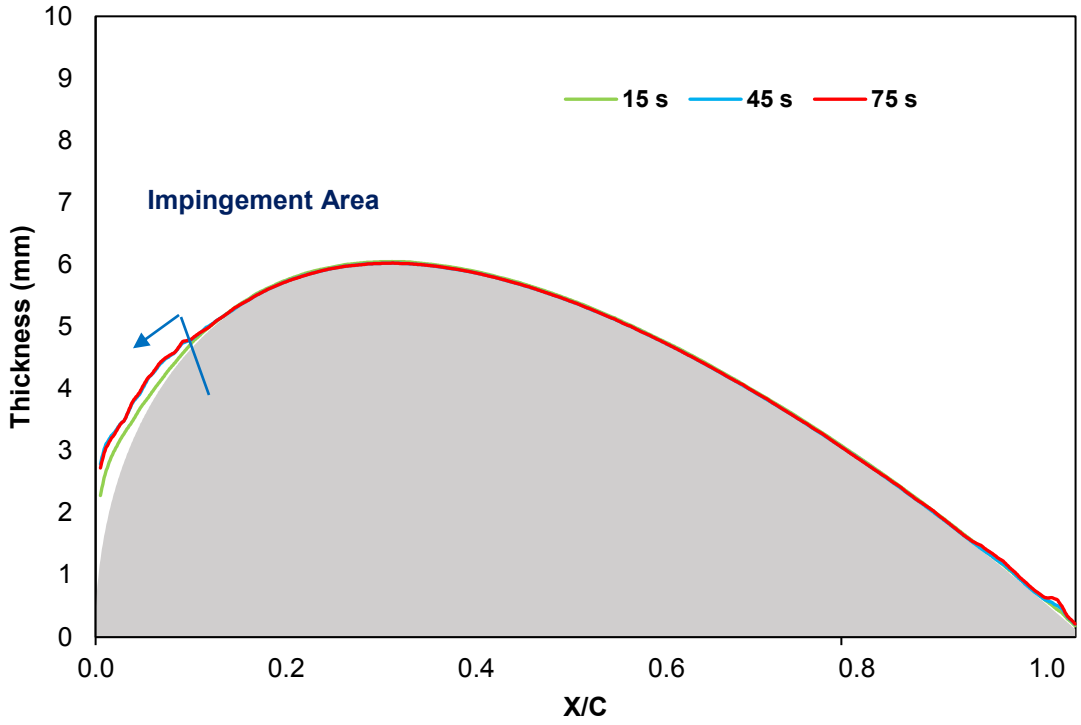

Figure 3-15: Ice/water thickness evolution by time for Al/20/-15.

3.2.4 Chord-Wise Distribution

Another type of comparison is for different temperatures, speeds, and surfaces at the same time. The raw images are shown in Figure 3-16 for t= 30 s, while the results for a span-wise average of the ROI are available in Figure 3-17 and Figure 3-18. In these figures, the horizontal axis is the arc length of the airfoil along the chord-wise direction. As an overall result, the spread on the superhydrophobic surface seems less than on the aluminium and, therefore, more ice accumulates around the leading edge region. It should be noted that, it is impossible to talk about the amount of ice confidently, because there is no information for ice upstream of the leading edge. With decreasing the temperature, more ice accretes on the leading edge, therefore less ice runs back. Since the surface energy of the superhydrophobic coating is low, less water is absorbed by the surface downstream of the impingement area and thus less ice forms there. However, droplets tend to stick to the superhydrophobic surface in the impingement area, more likely in reduced temperatures. This behaviour may originate from the fact that the order of size of the droplets and surface roughness are almost the same. Consequently, after the first layer of ice forms on the

superhydrophobic surface, it is no longer water repellent and absorbs more droplets. As the speed increases, more droplets impact the surface and eventually lead to more ice accretion. Because of more drag force caused by speed, a greater area is covered by ice.

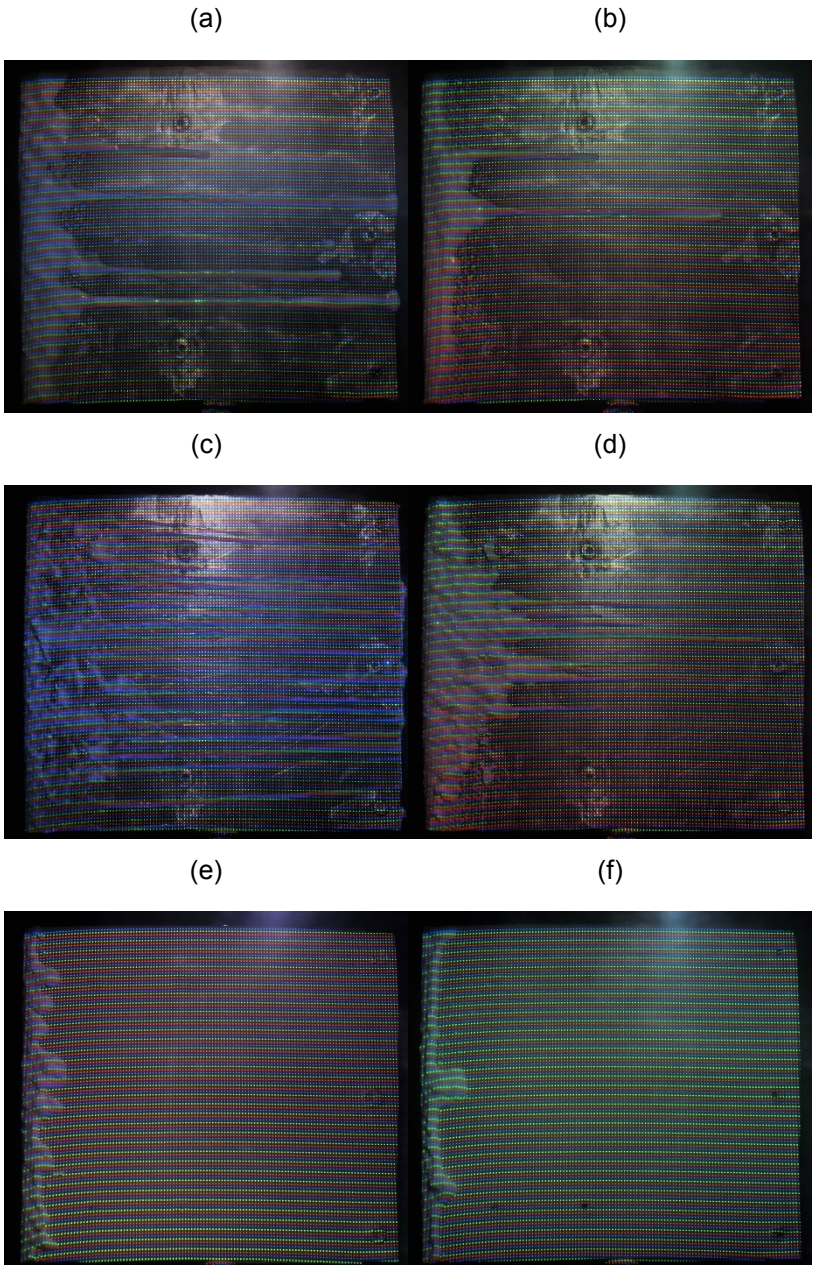

Figure 3-16: Raw images at t= 30 s. (a) for Al/20/-3.5, (b) for Al/20/-7, (c) for Al/40/-3.5, (d) for Al/40/-7, (e) for SH/20/-3.5, and (f) for SH/20/-7.

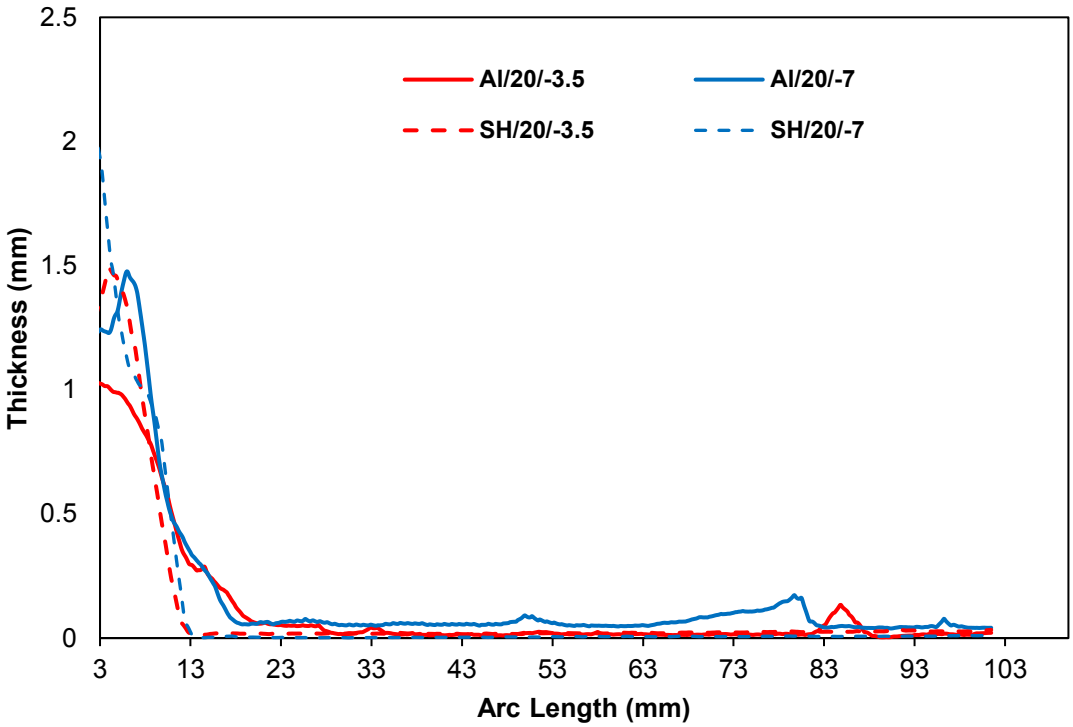

Figure 3-17: Ice thickness along the airfoil's surface in different temperatures and surfaces at t= 30s.

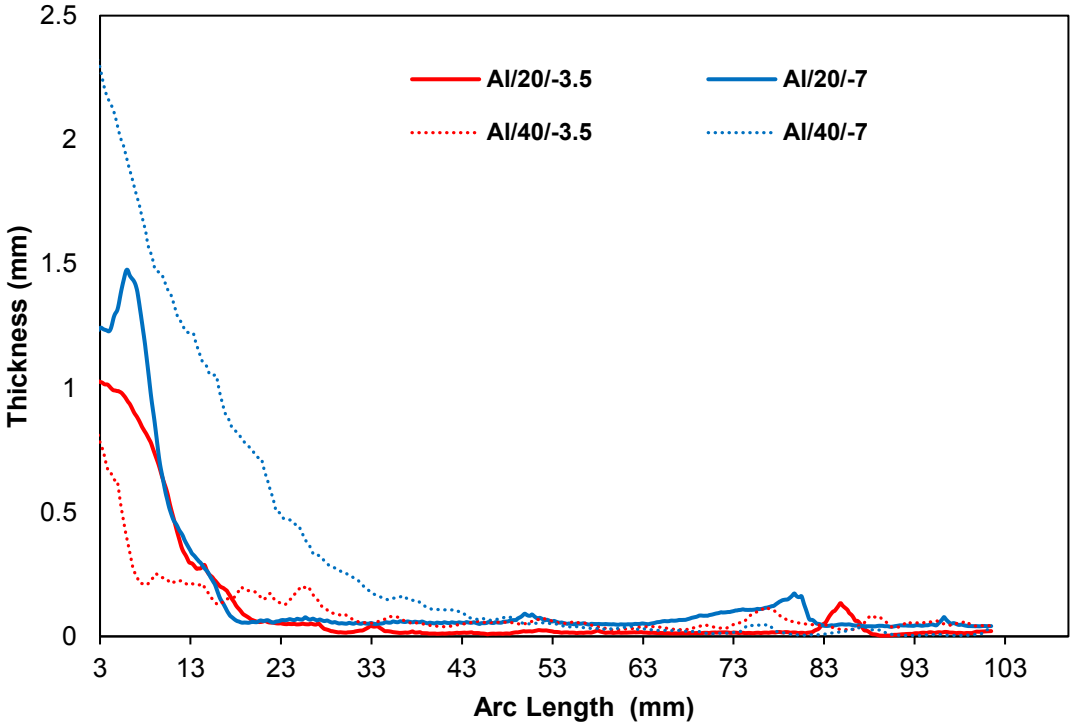

Figure 3-18: Ice thickness along the airfoil's surface in different temperatures and speeds at t= 30s.

While ice thickness information helps us to understand the most probable location of ice accretion, the growth rate provides information about the rate of ice accumulation. This information in a period of 30 s is provided in Figure 3-19, which compares different temperatures, speeds, and surfaces. Falling temperatures and increasing speeds increase the thickness growth, while the superhydrophobicity effect makes the profile more concentrated around the leading edge region.

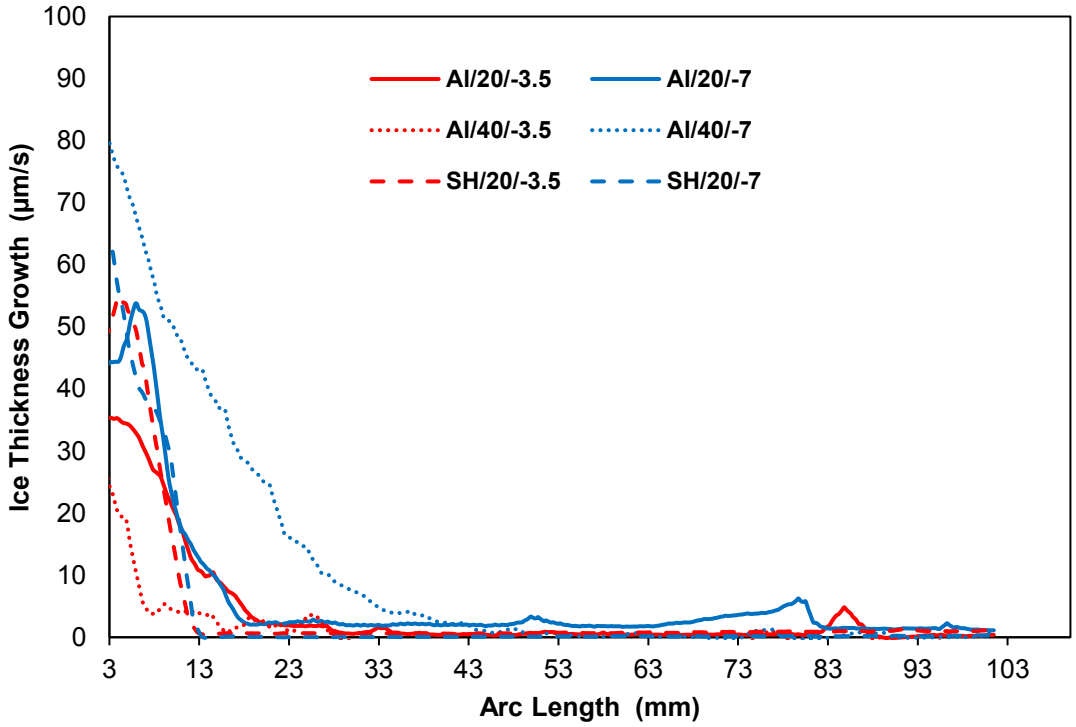

Figure 3-19: Ice thickness growth along the airfoil's surface in different temperatures, speeds, and surfaces in 30 s.

3.2.5 Ice Limit Tracking

If the ice limit (as shown in Figure 3-20) is defined as the most downstream location with a thickness more than a specific threshold, the comparison of ice movement is possible. The ice limit can be found by sweeping the span-wise average profile from the trailing edge (X/C= 1) toward the leading edge and looking for the first thickness value more than 500 µm. This comparison is shown in Figure 3-21 and Table 3-1 in the ROI up to t= 60 s. On the aluminium surface and at the lower velocity, the ice limit advances gradually, and then shedding occurs in the lower temperature case. On the aluminium surface and at the higher velocity, the advance is almost

uniform but steeper in the lower temperatures, while shedding is seen in the higher temperature experiment. On the superhydrophobic surface, the advance is almost independent of the temperature. On the aluminium surface, falling temperatures and increasing speeds have almost the same effect on ice limit location.

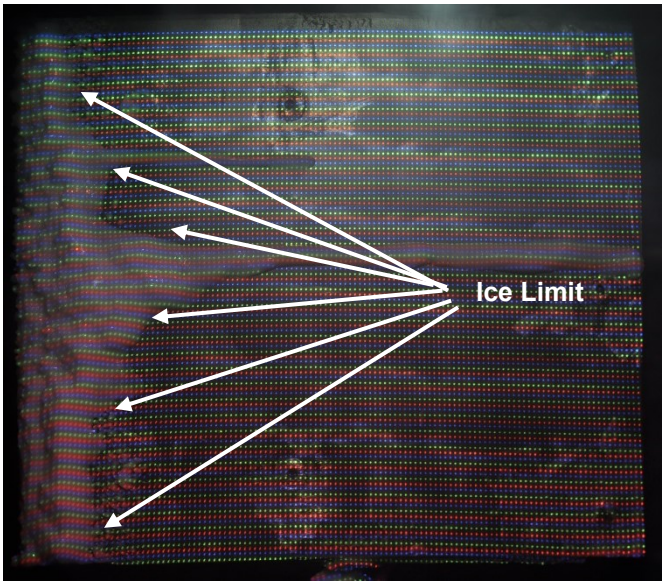

Figure 3-20: Ice limit definition.

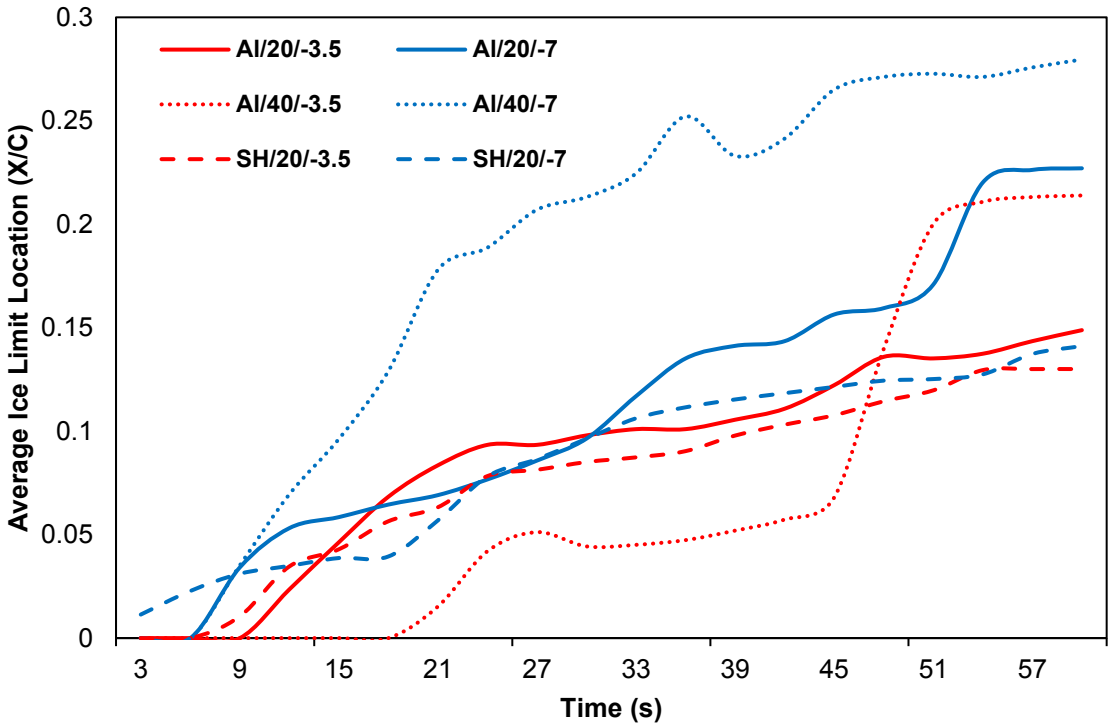

Figure 3-21: Ice limit movement at different icing conditions.

Table 3-1: Ice limit movement speed and location at t= 60 s.

Experiment	Average Velocity (µm/s)	Final Ice limit Location (X/C)			
		Average	Min.	Max.	STD
Al/20/-3.5	275	0.44	0.13	1	0.35
Al/20/-7	398	0.44	0.13	1	0.37
Al/40/-3.5	532	0.33	0.11	0.89	0.20
Al/40/-7	501	0.38	0.19	0.89	0.13
SH/20/-3.5	337	0.14	0.06	0.18	0.05
SH/20/-7	239	0.12	0.09	0.17	0.04

3.2.6 Mass Balance

The amount of collected water is another parameter that can be extracted from the thickness profile, and it is a useful tool for comparing different surfaces. This parameter is shown in Figure 3-22 in a period of 60 s for a region with 20% of the width of the span around the centreline. As deduced before, at T= 0ºC, the flow on the airfoil is in the liquid phase, and, therefore, the

amount of collected water is almost constant. On the other hand, when the condition is favourable for forming ice, more water is collected by the airfoil surface, and the collection rate relates directly to temperature and speed. As expected, the curves for the superhydrophobic surface are under those for aluminium. The overall water collection rate is shown in Table 3-2, in which it is clearly stated that the superiority of the superhydrophobic surface is reduced in icing conditions. It should be noted that these values are without the amount accreted upstream of the leading edge.

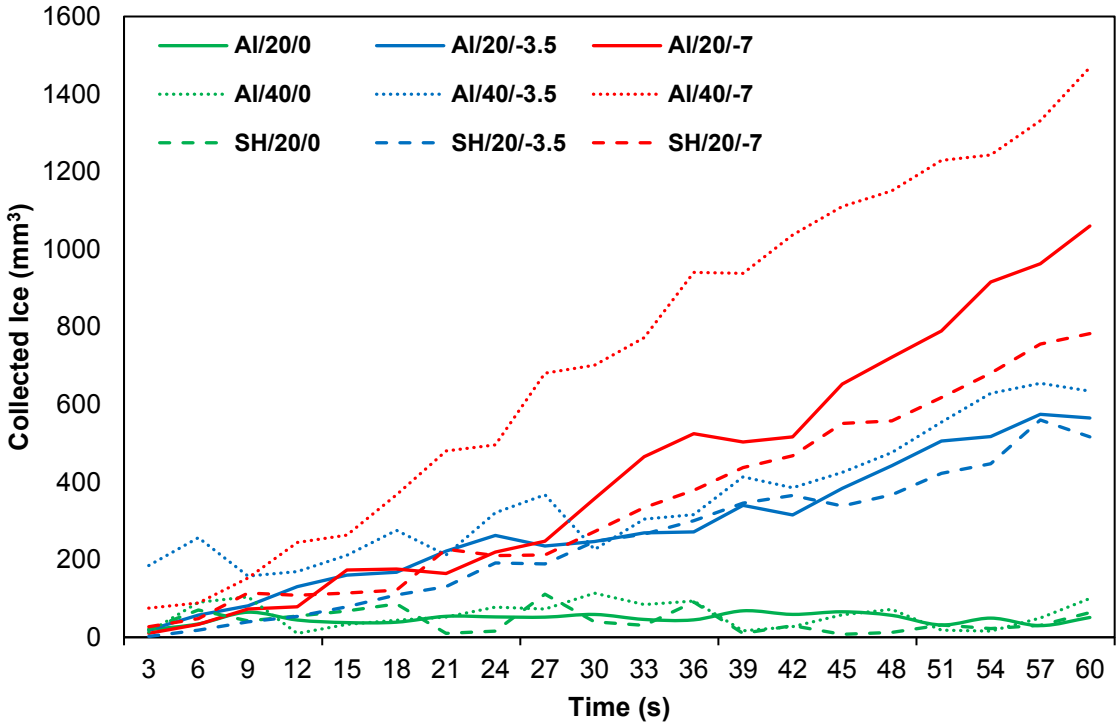

Figure 3-22: Collected ice on the airfoil in different icing conditions.

Table 3-2: Collected ice quantities.

Experiment	Collection Rate (mm^3/s)	Final Accumulated Ice/Water (mm^3)
Al/20/0	---	51
Al/20/-3.5	27	565
Al/20/-7	44	1060
Al/40/0	---	100
Al/40/-3.5	32	634
Al/40/-7	71	1468
SH/20/0	---	64
SH/20/-3.5	24	516
SH/20/-7	35	783

3.2.7 Runback Tracking

Another useful practice is runback tracking. As shown in Figure 3-23, a runback was formed at a time between t= 27s and t= 30 s on Y/S= -0.08 for Al/20/-7, and it continued to extend and grow. The evolution of this runback at different times is depicted in Figure 3-24. In this figure, the horizontal axis is the arc length of the airfoil along the chord-wise direction. The formation of two nucleation sites at Y/C= 0.5 and Y/C= 0.8 is clear. They were absorbing more droplets from the air stream and growing. If the goal of the experiment is studying the runback rivulets and checking whether they reach the control surfaces or not, this kind of analysis is helpful.

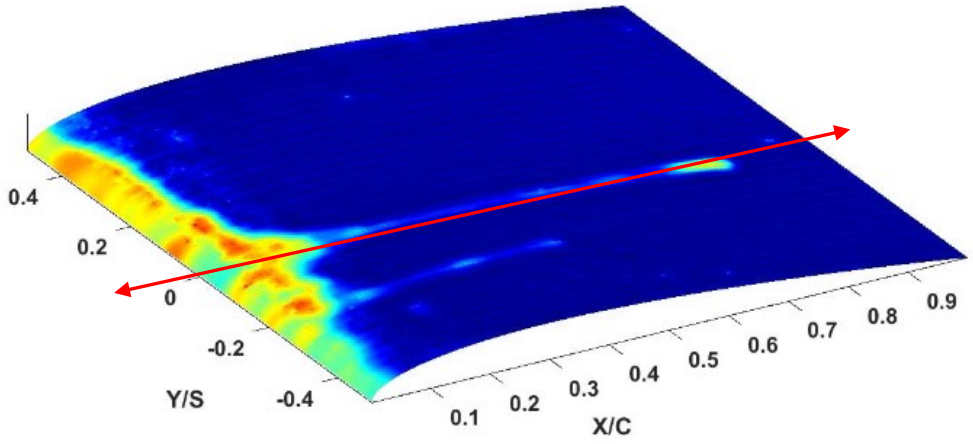

Figure 3-23: Runback formation on the aluminium surface.

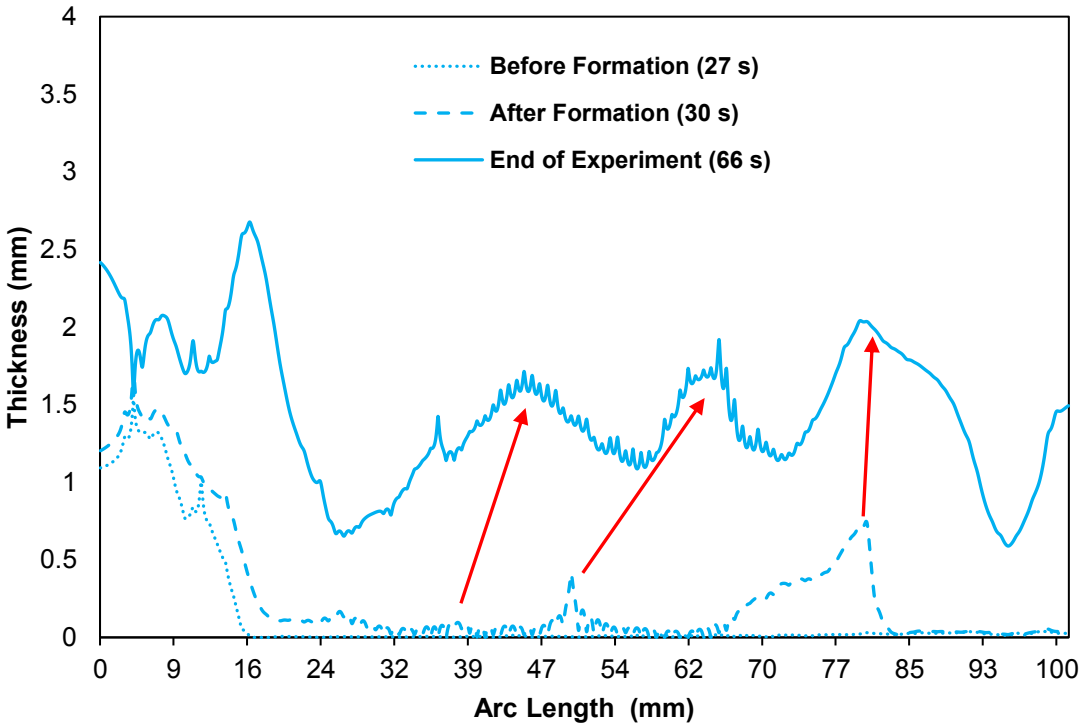

Figure 3-24: Runback evolution.

4 Closure

4.1 Summary and Conclusion

The goal of this project was to develop and assess a novel non-instructive method for measuring the thickness of water and ice. For this purpose, the concept of Digital Image Projection (DIP) was implemented first. After becoming acquainted with its limitations, some modifications were carried out to improve its thickness measurement range. Finally, a novel Colour Coded Point Projection (CCPP) method was introduced to eliminate the problems of overlapping and improve thickness measurement range and planar resolution. In this method, planar resolution is tripled in comparison with the DIP. After gathering the required equipment, completing the experimental setup, and implementing the CCPP concept, measurement of a single droplet proved the capability of the proposed method.

Then the technique was characterised to have a comprehensive understanding of its requirements, limitations, and accuracy. The results of the image quality test showed that the image SNR needs to be at least 4 to make sure that this method can capture the features successfully. Although this method can work well with solid objects, the light penetration problem is an issue for liquids. A test was done to quantise this limitation and the errors involved. It was shown that measurements of more than 600 microns have errors of less than 10%, while the minimum recognisable thickness is 50 microns. These two limitations are due to the equipment, setup configuration, and the material used to colourize the water, not the concept. If the object under

study is thicker than the minimum threshold, this methods provides a simple and accurate measurement tool.

Several experiments were conducted, on aluminium and a superhydrophobic surface at different airspeeds and temperatures, to make sure of the usefulness of the proposed method in real wind tunnel experiments. The thickness profile of different phenomena, like water rivulets and ice accretion, was captured successfully. It was found that the current equipment is not suitable for measuring small thicknesses, like film and rivulets. However, upgrading the equipment can eliminate this limitation. By extracting different information, like chord-wise thickness, ice growth rate, ice limit and advancement speed, and ice collection rate, from the reconstructed profile, the experiments were compared with each other quantitatively. It was found that the ice tends to accumulate on locations closer to the leading edge at lower temperatures. The same trend was seen on the superhydrophobic surfaces, even at higher temperatures. The study of ice front velocity showed that more advancement rate on the aluminium surface is at lower temperatures, while the trend is reverse on the superhydrophobic surface. The comparison of the rate of water collection on different surfaces also showed that less ice accumulated on the superhydrophobic surface. However, this amount is not so much that prove that a superhydrophobic surface is icephobic too.

In conclusion, the proposed novel method proved the practical ability of measuring the water and ice thickness in icing wind tunnel experiments. By providing the three-folded planar resolution, it could measure objects with a wider thickness variation with the same equipment. It tried to fill the gap among the practical thickness measurement tools by providing the accuracy of 90% for thicknesses over 600 microns. Since the results are valid for slightly aft the leading edge of the airfoil to the trailing edge, its main application in wind tunnel experiments may be analysing the flow in wet regime in ice protection systems. Due to the feasibility and potential of providing different information about ice geometry, it is a valuable tool for future researches.

4.2 Recommendations for Future Work

What has been done in the present thesis can be considered as developing the basis of a new measurement tool and paving the path for future researchers. It built the foundation for those

who want to either improve the method or use it as a tool. Therefore, in this section, some recommendation are provided for both groups.

- The angle between the optical axis of the projector and the camera can affect the amount of the points' displacement for a specific thickness. It should be adjusted correctly regarding the other specifications of the setup. Although smaller angles provide less displacement and, hence, a finer grid can be used, the amount of light penetration will increase and the sensitivity will drop.
- The contrast and the brightness of the projector must be set according to the sensitivity of camera. Although higher brightness provides a greater light intensity of the liquid surface, it will saturate a bigger region of the camera's sensor. The overall effect will force us to use a coarser grid pattern to eliminate the overlapping problem. One remedy may be using a shorter exposure time, e.g., higher shutter speed.
- It is highly recommended to use an industrial camera instead of a DSLR one. In this situation, more control of the imaging parameters will be available.
- Regarding the tandem projection of the colours in DLP projectors, synchronising it with the camera is essential. Using an LCD projector with sufficient brightness and smaller pixel size will be the optimum case.

The recommendations above may guide those who wish to use this method. However, for those who want to improve this technique, the following areas are suggested.

- Assess the effect of pigments that can provide maximum opacity while having minimal effect on the physical properties of the water.
- Study the feasibility of working in the infrared or ultraviolet region of the electromagnetic spectrum to eliminate the necessity of adding pigment to the water.

Regardless of the limitations of the proposed method, it can provide different information at low cost. Therefore, the following topics can be studied further using this technique.

- Study the dynamic behaviour of rivulets using high-speed imaging.

- Study ice formation on wet ice protection systems.
- Compare different types of superhydrophobic and icephobic coatings.
- Assess the possibility of distinguishing between types of ice.
- Assess the possibility of using this method on real wings in flight conditions.

Bibliography

[1] D. Eick, "Aircraft Icing Accidents," Washington, DC, 2015.

[2] R. J. Ranaudo, J. G. Batterson, A. L. Reehorst, T. H. Bond, and T. M. O'Mara, "Effects of Horizontal Tail Ice on Longitudinal Aerodynamic Derivatives," *J. Aircr.*, vol. 28, no. 3, pp. 193–199, 1991.

[3] Federal Aviation Administration, "Pilot Guide: Flight in Icing Conditions," 2015.

[4] M. B. Bragg, G. M. Gregorek, and J. D. Lee, "Airfoil Aerodynamics in Icing Conditions," *J. Aircr.*, vol. 23, no. 1, pp. 76–81, 1986.

[5] P. J. Perkins and W. J. Rieke, *In-Flight Icing*, 2nd ed. Sporty's Pilot Shop, 2001.

[6] N. Czernkovich, "Understanding In-Flight Icing," in *Transport Canada Aviation Safety Seminar*, 2004.

[7] B. Robichaud and J. Mullock, *The Weather of Atlantic Canada and Eastern Quebec Graphic Area Forecast 34*. NAV CANADA, 2000.

[8] A. Dolatabadi, "Ice-Phobic Evaluation of Super-Hydrophobic Coatings for Aircaft Icing Protection," *Montr. PWC*, 2010.

[9] B. Wang, F. W. Lohry, S. Zhang, and H. Hu, "Development of a Digital Fringe Projection

Technique to Characterize the Transient Behavior of Wind-Driven Droplet/ Rivulet Flows," in *50th AIAA Aerospace Sciences Meeting including the New Horizons Forum and Aerospace Exposition*, 2012.

[10] W. Olsen and E. Walker, "Experimental Evidence for Modifying the Current Physical Model for Ice Accretion on Aircraft Surfaces," 1986.

[11] H. E. Huppert, "Flow and Instability of a Viscous Current Down a Slope," *Nature*, vol. 300, 1982.

[12] L. M. Hocking, W. R. Debler, and K. E. Cook, "The Growth of Leading-Edge Distortions on a Viscous Sheet," *Phys. Fluids*, vol. 11, no. 2, pp. 307–313, 1999.

[13] G. McAlister, R. Ettema, and J. S. Marshall, "Wind-Driven Rivulet Breakoff and Droplet Flows in Microgravity and Terrestrial-Gravity Conditions," *J. Fluids Eng.*, vol. 127, no. 2, p. 257, 2005.

[14] A. M. Cazabat, F. Heslot, S. M. Troian, and P. Carles, "Fingering Instability of Thin Spreading Films Driven by Temperature Gradients," *Nature*, vol. 346, pp. 818–822, 1990.

[15] T. Ward, C. Wey, R. Glidden, A. E. Hosoi, and A. L. Bertozzi, "Experimental Study of Gravitation Effects in the Flow of a Particle-Laden Thin Film on an Inclined Plane," *Phys. Fluids*, vol. 21, no. 8, 2009.

[16] J. R. de Bruyn, "Growth of Fingers at a Driven Three-Phase Contact Line," *Phys. Rev. A*, vol. 46, no. 8, 1992.

[17] F. Melo, J. F. Joanny, and S. Fauve, "Fingering Instability of Spinning Drops," *Phys. Rev. Lett.*, vol. 63, no. 18, pp. 1958–1961, 1989.

[18] R. J. Hansman and A. P. Craig, "Low Reynolds Number Tests of NACA 64-210, NACA 0012, and Wortmann FX67-K170 Airfoils in Rain," *J. Aircr.*, vol. 24, no. 8, pp. 559–566, 1987.

[19] V. V. Lel, F. Al-Sibai, A. Leefken, and U. Renz, “Local Thickness and Wave Velocity Measurement of Wavy Films with a Chromatic Confocal Imaging Method and a Fluorescence Intensity Technique,” *Exp. Fluids*, vol. 39, no. 5, pp. 856–864, 2005.

[20] A. Benetazzo, “Measurements of Short Water Waves Using Stereo Matched Image Sequences,” *Coast. Eng.*, vol. 53, no. 12, pp. 1013–1032, 2006.

[21] J. Eaket, F. E. Hicks, and A. E. Peterson, “Use of Stereoscopy for Dam Break Flow Measurement,” *J. Hydraul. Eng.*, vol. 131, no. 1, pp. 24–29, 2005.

[22] R. Tsubaki and I. Fujita, “Stereoscopic Measurement of a Fluctuating Free Surface with Discontinuities,” *Meas. Sci. Technol. Stereosc.*, vol. 16, 2005.

[23] J. M. Wanek and C. H. Wu, “Automated Trinocular Stereo Imaging System for Three-Dimensional Surface Wave Measurements,” *Ocean Eng.*, vol. 33, no. 5–6, pp. 723–747, 2006.

[24] S. Van der Jeught and J. J. J. Dirckx, “Real-Time Structured Light Profilometry: A Review,” *Opt. Lasers Eng.*, vol. 87, no. 2016, pp. 18–31, 2016.

[25] S. S. Gorthi and P. Rastogi, “Fringe Projection Techniques: Whither We Are?,” *Opt. Lasers Eng.*, vol. 48, no. 2, pp. 133–140, 2010.

[26] Q.-C. Zhang and X.-Y. Su, “An Optical Measurement of Vortex Shape at a Free Surface,” *Opt. Laser Technol.*, vol. 34, no. 2, pp. 107–113, 2002.

[27] O. Pouliquen and Y. Forterre, “Friction Law for Dense Granular Flows: Application to the Motion of a Mass Down a Rough Inclined Plane,” *J. Fluid Mech.*, vol. 453, pp. 133–151, 2002.

[28] S. Cochard and C. Ancey, “Tracking the Free Surface of Time-Dependent Flows: Image Processing for the Dam-Break Problem,” *Exp. Fluids*, vol. 44, no. 1, pp. 59–71, 2008.

[29] P. J. Cobelli, A. Maurel, V. Pagneux, and P. Petitjeans, “Global Measurement of Water

Waves by Fourier Transform Profilometry," *Exp. Fluids*, vol. 46, no. 6, pp. 1037–1047, 2009.

[30] G. L. Kouyi, J. Vazquez, and J. B. Poulet, "3D Free Surface Measurement and Numerical Modelling of Flows in Storm Overflows," *Flow Meas. Instrum.*, vol. 14, no. 3, pp. 79–87, 2003.

[31] J. Liu, S. J.B., and J. P. Gollub, "Three-Dimensional Instabilities of Film Flows," *Phys. Fluids*, vol. 7, no. 55, pp. 55–67, 1995.

[32] M. F. G. Johnson, R. A. Schluter, and S. G. Bankoff, "Fluorescent Imaging System for Global Measurement of Liquid Film Thickness and Dynamic Contact Angle in Free Surface Flows," *Rev. Sci. Instrum.*, vol. 68, no. 11, pp. 4097–4102, Nov. 1997.

[33] M. F. G. Johnson, R. A. Schluter, M. J. Miksis, and S. G. Bankoff, "Experimental Study of Rivulet Formation on an Inclined Plate by Fluorescent Imaging," *J. Fluid Mech.*, vol. 394, pp. 339–354, 1999.

[34] E. A. Chinnov, S. M. Kharlamov, A. V. Saprykina, and O. V. Zhukovskaya, "Measuring Deformations of the Heated Liquid Film by the Fluorescence Method," *Thermophys. Aeromechanics*, vol. 14, no. 2, p. 241-246--, 2007.

[35] A. Schagen and M. Modigell, "Local Film Thickness and Temperature Distribution Measurement in Wavy Liquid Films with a Laser-Induced Luminescence Technique," *Exp. Fluids*, vol. 43, no. 2–3, pp. 209–221, 2007.

[36] C. H. Hidrovo and D. P. Hart, "Emission Reabsorption Laser Induced Fluorescence (ERLIF) Film Thickness Measurement," *Meas. Sci. Technol.*, vol. 12, no. 4, p. 467, 2001.

[37] W. B. Wright, R. Budakian, and S. J. Putterman, "Diffusing Light Photography of Fully Developed Isotropic Ripple Turbulence," *Phys. Rev. Lett.*, vol. 76, no. 24, pp. 4528–4531, 1996.

[38] X. Zhang, D. Dabiri, and M. Gharib, "Optical Mapping of Fluid Density Interfaces :

Concepts and Implementations," *Rev. Sci. Instrum.*, vol. 1858, no. 67, 1996.

[39] O. A. Kabov, B. Scheid, I. A. Sharina, and J.-C. Legros, "Heat Transfer and Rivulet Structures Formation in a Falling Thin Liquid Film Locally Heated," *Int. J. Therm. Sci.*, vol. 41, no. 7, pp. 664–672, 2002.

[40] F. Moisy, M. Rabaud, and K. Salsac, "A Synthetic Schlieren Method for the Measurement of the Topography of a Liquid Interface," *Exp. Fluids*, vol. 46, no. 6, pp. 1021–1036, 2009.

[41] R. Savelsberg, A. Holten, and W. Van De Water, "Measurement of the Gradient Field of a Turbulent Free Surface," *Exp. Fluids*, vol. 41, no. 4, pp. 629–640, 2006.

[42] A. G. Pautsch and T. A. Shedd, "Adiabatic and Diabatic Measurements of the Liquid Film Thickness During Spray Cooling with FC-72," *Int. J. Heat Mass Transf.*, vol. 49, no. 15–16, pp. 2610–2618, 2006.

[43] K. Zhang, S. Zhang, A. Rothmayer, and H. Hu, "Development of a Digital Image Projection Technique to Measure Wind-Driven Water Film Flows," *Am. Inst. Aeronaut. Astronaut.*, 2013.

[44] K. Zhang, T. Wei, and H. Hu, "An experimental investigation on the surface water transport process over an airfoil by using a digital image projection technique," *Exp. Fluids*, vol. 56, no. 9, pp. 1–16, 2015.

[45] K. Zhang and H. Hu, "An Experimental Study of the Wind-Driven Water Droplet/Rrivulet Flows Over an Airfoil Pertinent to Wind Turbine Icing Phenomena," pp. 1–13, 2016.

[46] J. P. Lewis, "Fast Normalized Cross-Correlation," *Vis. Interface*, vol. 10, no. 1, pp. 120–123, 1995.

[47] C. Gendrich and M. Koochesfahani, "A spatial correlation technique for estimating velocity fields using molecular tagging velocimetry (MTV)," *Exp. Fluids*, vol. 22, no. 2, pp. 67–77, 1996.

[48] MathWorks, "normxcorr2." [Online]. Available: https://www.mathworks.com/help/images/ref/normxcorr2.html.

[49] A. Przadka, B. Cabane, V. Pagneux, A. Maurel, and P. Petitjeans, "Fourier transform profilometry for water waves: How to achieve clean water attenuation with diffusive reflection at the water surface?," *Exp. Fluids*, vol. 52, no. 2, pp. 519–527, 2012.